Broadband acoustic inversion for gas flux quantification - application to a methane plume at Scanner Pockmark, central North Sea

Jianghui Li[1], Ben Roche[2], Jonathan M. Bull[2], Paul R. White[1], Timothy G. Leighton[1], Giuseppe Provenzano[2], Marius Dewar[3], Tim J. Henstock[2]

[1]Institute of Sound and Vibration Research, University of Southampton, Southampton, SO17 1BJ, U.K.
[2]Ocean and Earth Science, University of Southampton, National Oceanography Centre, Southampton, SO14 3ZH, U.K.
[3]Plymouth Marine Laboratory, Prospect Place, Plymouth, PL1 3DH, U.K.

Key Points:

- A new method for determining the bubble size distribution and gas flow rate of gas plumes in the water column is presented utilising active acoustic data with a broad bandwidth (3.5-200 kHz).
- Imaging of the methane plume emerging from the Scanner Pockmark in the North Sea showed that it comprised two distinct arms.
- The upper plume arm comprises larger gas bubbles with radii ranging from 1 mm to 15 mm, while the lower arm comprises smaller gas bubbles with radii ranging from 0.01 mm to 0.15 mm.
- Total *in situ* methane flux from the pockmark into the water column is quantified as between 1.6 to 2.7 $\times 10^6$ kg/year (272 to 456 L/min).

Corresponding author: Jianghui Li, `e-mail:J.Li@soton.ac.uk`

This article has been accepted for publication and undergone full peer review but has not been through the copyediting, typesetting, pagination and proofreading process which may lead to differences between this version and the Version of Record. Please cite this article as doi: 10.1029/2020JC016360

Abstract

The release of greenhouse gases from both natural and man-made sites has been identified as a major cause of global climate change. Extensive work has addressed quantifying gas seeps in the terrestrial setting while little has been done to refine accurate methods for determining gas flux emerging through the seabed into the water column. This paper investigates large scale methane seepage from the Scanner Pockmark in the North Sea with a new methodology which integrates data from both multibeam and single-beam acoustics, with single-beam data covering a bandwidth (3.5 to 200 kHz) far wider than that used in previous studies, to quantify the rate of gas release from the seabed into the water column. The multibeam data imaged a distinct fork shaped methane plume in the water column, the upper arm of which was consistently visible in the single-beam data while the lower arm was only intermittently visible. Using a novel acoustic inversion method we determine the depth-dependent gas bubble size distribution and the gas flux for each plume arm. Our results show that the upper plume arm comprises bubbles with radii ranging from 1 mm to 15 mm, while the lower arm consists of smaller bubbles with radii ranging from 0.01 mm to 0.15 mm. We extrapolate from these estimates to calculate the gas flux from the Scanner Pockmark as between 1.6 and 2.7×10^6 kg/year (272 to 456 L/min). This range was calculated by considering uncertainties together with Monte Carlo simulation. Our improved methodology allows more accurate quantification of natural and anthropogenic gas plumes in the water column.

Plain Language Summary

Understanding the rate of gas release from natural ebullition sites, such as pockmarks, into the water column is a major factor in understanding the input of greenhouse gases, such as methane and carbon dioxide, into the global ocean system. The detection and quantification of gas flux in the marine environment have relied upon acoustics. However, current active acoustic methods are fairly based on single frequency quantification, which can never unambiguously quantify the gas flux due to the bubble size distribution and the scattering across a range of frequencies, lead to an ill-conditioned inversion problem. This paper proposes a solution to this dilemma using two elements. Firstly, we employ a wider range of frequencies than previously used, so that more of the bubble resonances are encompassed. Secondly, it assumes a form for the bubble size distribution, further constraining the solution and effectively regularising the inversion. The broadband methodology enables us to quantify gas flux with frequencies spanning the resonances of all the bubbles in the plume, allowing more accurate quantification of natural and anthropogenic gas plumes in the water column.

1 Introduction

Understanding the rate of gas release from natural ebullition sites, such as pockmarks, into the water column is a major factor in understanding the input of greenhouse gases, such as methane (CH_4) and carbon dioxide (CO_2), into the global ocean system (Ligtenberg & Connolly, 2003; Leifer & Boles, 2005; McGinnis et al., 2006; Kennett et al., 2003; Greinert, McGinnis, et al., 2010; Shakhova et al., 2010). The detection and quantification of gas flux in the marine environment have relied upon methods of passive (Leighton & White, 2011; B. J. Berges et al., 2015; Blackford et al., 2014; Li, White, Roche, et al., 2019; Li et al., 2020) and active (Riedel et al., 2018; Veloso et al., 2015; von Deimling et al., 2011; Leblond et al., 2014; Westbrook et al., 2009; Greinert, Lewis, et al., 2010; Greinert et al., 2006; Greinert & Nützel, 2004; Ostrovsky, 2003; Nikolovska & Schanze, 2007; Shakhova et al., 2014; G. Xu et al., 2014; Rona & Light, 2011; Li, White, Bull, Leighton, & Roche, 2019) acoustics. These two methods are largely complementary with passive acoustics well suited to long-term and local monitoring of small sites allowing quantification, whereas active acoustics survey equipment is widely available and able to detect gas over a large spatial area, but is less well adapted to quantification.

Active acoustics, specifically the use of multibeam echosounders, has been commonly used for seep detection in the last decades (Greinert, Lewis, et al., 2010; C. Xu et al., 2020) and has been used to map both natural and anthropogenic ebullition sites worldwide (Urban et al., 2017; Greinert, Lewis, et al., 2010; Greinert et al., 2006; Westbrook et al., 2009; Leblond et al., 2014; von Deimling et al., 2015; Nikolovska et al., 2008; Ostrovsky, 2003; Ostrovsky et al., 2008). Echosounders also have the advantage of being able to work in any body of water regardless of visibility unlike optical techniques. Gas seeps in sonar data commonly appear as readily identifiable medium/strong reflectors - within the water column, sometimes referred to as “gas flares”. Using multibeam echosounders the position and shape of these flares can be mapped (Urban et al., 2017; Greinert, Lewis, et al., 2010). By mapping the shape of these flares, observing the angle they make with the seabed, and knowing the tidal velocity one can predict the vertical velocity of the bubble cloud. There is a simple relationship between ascent velocity and bubble size, and hence the dominant bubble size can be estimated (Toramaru, 1989).

In order to gain an estimate of gas flux via active acoustics, single-beam (single frequency) echosounder data has been used (Veloso et al., 2015; von Deimling et al., 2010; Römer et al., 2014; Shakhova et al., 2015; Greinert, McGinnis, et al., 2010; Bayrakci et al., 2014). This is done by first modelling the theoretical return pulse strength from bubbles of different sizes based on the frequency of the acoustic source and the depth of water in the area. Then by observing the mean signal strength from within the plume an estimate of bubble size distribution can be made. Crucially, this can only be done if the ambiguity is ignored, since when a given scattering strength is attributed to a bubble, there is always more than one bubble size that can scatter that frequency strongly (Leighton et al., 2004). Consequently there is an inherent ambiguity in the gas flux estimated by a technique which only uses data containing a single frequency. This ambiguity exists even when only a single bubble is being measured in free field (Leighton et al., 1996), and becomes much greater if there are many bubbles (as here) or the bubbles are contained within a structure (Leighton et al., 2012; Baik et al., 2014). From this distribution the flux of the plume can be estimated (carrying forward any inherent ambiguity) using the calculated rise speeds of bubbles (Greinert & Nützel, 2004; Greinert et al., 2006; Greinert, Lewis, et al., 2010; Leblond et al., 2014; Nikolovska & Schanze, 2007). Greinert et al. (Greinert et al., 2006) used both single- and multibeam data to estimate the dominant bubble size at different depths in the water column. This method has also been used to make observations of the temporal variations of plumes and their interaction with the thermocline (von Deimling et al., 2015). However, the modelling used in this method requires very accurate measurement of water column physical properties as well as bubble rise velocity.

In an attempt to establish a technique to directly quantify gas flux from active acoustic data, Greinert and Nützel (Greinert & Nützel, 2004) demonstrated that (within the confines of a specific seep, constrained to remove the inherent ambiguity in the acoustic inversion) there is a direct relationship between the volume backscattering strength of a single-beam pulse and the flux rate of a seep, using a controlled release site and a horizontal acoustic array. However, this relationship varies with the dominant bubble size meaning it is site-specific, and must be re-established at every new seep via empirical measurements (Greinert & Nützel, 2004; Leblond et al., 2014). This approach was used by Nikolovska et al. (Nikolovska et al., 2008) in the Black Sea, using a Remotely Operated Underwater Vehicle (ROV) to collect physical flux measurements alongside a horizontally mounted sonar system, and by Bayrakci et al. (Bayrakci et al., 2014) in the Marmara Sea, using a rotating bubble detector (BOB) to reveal temporal variations in the gas flux of surrounding seeps. While this technique is appropriate for long term measurements of single seep sites, it is intrinsically flawed for widespread quantification of multiple seeps as an empirical measurement of flux is required to make such an estimate. Furthermore, it assumes that conditions do not change (e.g. significantly larger bubbles are introduced through a new fracture in the sediment or infrastructure casing) in such a way as to make the gas flux quantification erroneous through the above-mentioned ambiguity.

The existence of the inherent ambiguity is therefore probably the most significant shortcoming of the existing acoustic techniques, i.e. ebullition sites contain a bubble population with a wide range of radii (Veloso et al., 2015). Crucially, passive acoustic techniques do not contain inherent ambiguities in the acoustic inversion: they only contain acoustic uncertainties, which are less troublesome. To be specific, each bubble emits energy in a known frequency band relating to its size, depth, etc. The uncertainty in the amount of energy emitted by a given bubble being only a result of the paucity of data, which will be reduced as more data is taken (Leighton & White, 2011). In contrast, quantification of the gas flux by active sonar contains an inherent ambiguity, in that a given bubble can scatter strongly at resonance, and when it is also much larger than resonance (Leighton et al., 2004). As such, a single frequency echosounder can never unambiguously quantify the gas flux without additional measurements, e.g. passive acoustics, optical methods or gas collection using bottles, to remove the ambiguity. Measuring scattering across a range of frequencies which does not cover the resonant frequencies of the bubbles present, leads to an ill-conditioned inversion problem, i.e. the errors in the measurements are vastly magnified, leading to solutions which are unreliable. Physically relevant regularization of the solution is needed in order to provide usable solutions (Leighton et al., 1996).

Furthermore, the above mentioned active methods tend to rely upon scattering models for bubbles which assume the bubble is small relative to the insonifying wavelength. For the size of bubble that we are looking at and the frequencies of most imaging sonars, this condition is not true. This leads to errors in two ways: first, the calculation of the damping associated with each bubble, can be erroneous (Ainslie & Leighton, 2011, 2009); second, the assumed increase of scattering cross-section with increasing bubble size (a trend that is only valid for bubbles larger than resonance only do as long as the bubble radius remains much smaller than an acoustic wavelength) breaks down (Thuraisingham, 1997; Salomatin & Yusupov, 2005). Accurate determination of the bubble population, and hence gas flux, can only be determined if the backscatter response is determined for all significant bubble sizes, and this requires the use of a broad range of acoustic frequencies. Typical radii of bubbles emitted from the seabed tend to be in the range of 1 to 15 mm (Veloso et al., 2015) whose resonant frequencies are from 800 Hz to 12 kHz. While there is merit in using single frequency imaging (at for example 18 kHz (G. Xu et al., 2014)) to identify the location of seep sites, single frequency systems cannot determine the bubble population or the gas flux accurately. Even a multifrequency system that did not cover the range of bubble resonances (from below the resonant frequency of the largest bubble present, to above the frequency of the smallest bubble present) will contain inherent ambiguities, and if all the frequencies in a multibeam system are higher than the resonance of the larger bubble present (the convenient option given the frequencies in off-the-shelf multibeam sonars), then the equations in the simultaneous set mentioned above are not independent, and cannot be solved to determine the variables (the number of the bubbles in each size bin) unambiguously (Leighton & White, 2011; B. J. Berges et al., 2015). Currently, researchers have been using optical methods for quantification of small plumes such as a single bubble stream (Veloso et al., 2015), but this is impractical for analysing larger emission sites. Little work has been completed on quantifying the emissions from large methane plumes from active pockmarks which may extend over a diameter of 200 m in the water column, or understanding the gas bubble upwelling process.

This paper proposes a solution to this dilemma using two elements. Firstly, we employ a wider range of frequencies than previously used, so that more of the bubble res-

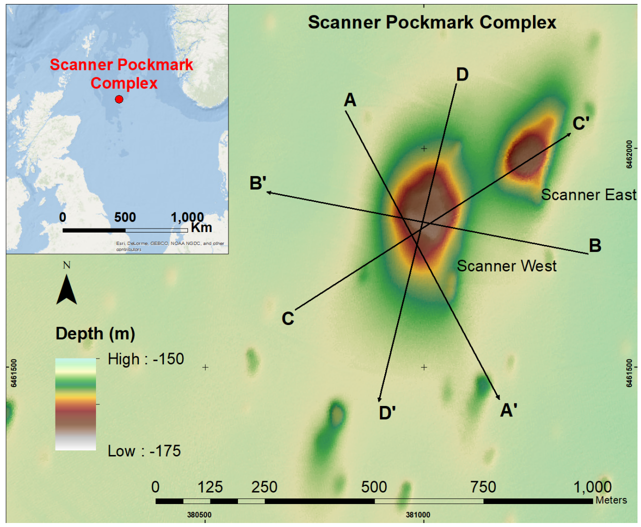

Figure 1: Bathymetric map of the Scanner Pockmark complex with inset showing the position within the central North Sea. The position of four ship profiles (A-D) which acoustically image the methane gas plume within the western pockmark are shown.

onances are encompassed. Secondly, it assumes a form for the bubble size distribution, further constraining the solution and effectively regularizing the inversion. We combine data from three sonar systems, spanning a wide frequency range, 2.5 kHz to 200 kHz, to calculate methane flux at an actively-venting pockmark in the North Sea. Scanner Pockmark complex comprises two large pockmarks (∼200-300 m in diameter, Figure 1) which are 15-20 m deep depressions in a relatively flat seabed in water depth of 150 m. Pockmarks are submarine gas escape structures commonly found in basins globally and often associated with active hydrocarbon systems. Despite first being observed in the 1960s, the variability and controls on gas emissions are poorly understood. The evolution of the resulting gas plumes in the water column is closely linked to the overall mechanism of gas leakage from pockmarks, making a greater understanding of plumes essential for better understanding natural seep sites. In order to determine the bubble size distribution of the gas plume and quantify the gas flux within it, we first use multibeam imaging to detect the plume structure and dimensions, then we present a volume scattering strength matching model utilizing iterations of bubble mean radii and standard deviation to match observed strength of single-beam data in the function of frequency ranging from 3.5 kHz to 200 kHz for each depth. Next, a sea current modulation function is applied to integrate the instantaneous bubble rise velocity, estimated at the time of observation. Finally we apply a depth-dependent number of bubbles and size distribution for methane gas to convert these volume flow rates to mass flow rates.

2 Data

The data in this survey were collected from the RRS James Cook during September, 2017. Three hull-mounted sonar systems were employed: a Konsberg EM710 multibeam echo sounder, a Konsberg SBP120 sub-bottom profiler and a Simrad EK60 single-beam echo sounder. The transceivers were orientated vertically downwards for the entire study. The EM710 multibeam echo sounder worked on frequency range 70 to 100 kHz with beamwidth of 1°. The SBP120 worked on a single-beam of wideband frequency (2.5-6.5 kHz) centred at ∼3.5 kHz with a beamwidth of 3°. The EK60 echosounder transmits a single-beam of five different monochromatic frequencies: 18, 38, 70, 120 and 200 kHz, with beamwidths of 11°, 7°, 7°, 7° and 7°, respectively. The pulse length of the SBP120 was set to 40 ms, and the pulse length of the EK60 at frequencies 18 kHz, 38 kHz, 70 kHz, 120 kHz and 200 kHz were set to 2048, 1024, 512, 256, and 256 μs, respectively. The multibeam data is used to observe the structure and dimensions of the plume while the sub-bottom profiler and single-beam data are used to measure the acoustic scattering properties of the plume. The sampling rate of the SBP120 and the EK60 were set to 20.48 kHz and 25 kHz respectively, which makes it possible for the target strength calculation in a reverberating volume V [m^3] with 1 m resolution in vertical.

2.1 EM710 multibeam data

The EK710 multibeam system imaged the methane plume from the western Scanner Pockmark. Figure 1 shows the transects across the plume. By filtering out background water column noise it was possible to extract the gas flare and recreate it as a 3-D model, recording its positional data, height, lateral extent and width, example results of this process are shown in Figure 2. The plume orientations are generally in good agreement with tidal direction, the axis of which runs roughly north to south, as predicted by Cazenave's FVCOM model (Cazenave et al., 2016). The plume height varies between 39-145 m above the seabed while the lateral spread varied between 5 and 210 m.

Over the recent decades, numerous methane plumes in different ocean regions have been investigated and the occurrence of multiple arms has been noted on several occasions (McGinnis et al., 2006; Gentz et al., 2014; von Deimling et al., 2015; Leifer et al., 2017; Sommer et al., 2015; Ruppel, 2011; Dissanayake et al., 2018). Examination of Figure 2 reveals that the plume selected here exhibits a clear forked structure with two distinct arms. This is presumed to be a result of two dominant bubble sizes escaping from the pockmark, with the larger bubbles rise faster, creating the upper arm while the smaller bubbles rise more slowly creating the lower arm.

The multibeam data also allows us to map the surrounding seafloor topography, revealing the Scanner Pockmark as being 10-20 m deeper than the surrounding seabed, which is at a depth of roughly 150 m (Figure 1). It was not possible to clearly map the plume within the crater due to the increased reverberation, likely caused by internal reflections and active gas venting.

2.2 SBP120 and EK60 single-beam data

Calibrated, single-beam data from the SBP120 and EK60 were collected along the transects A-D illustrated in Figure 1. Single-beam data at 18, 38, 70, 120, and 200 kHz was collected along the four profiles A-D across the Scanner Pockmark plume using an EK60 system with built-in calibration. This was augmented by data collected from a 3.5 kHz (2.5-6.5 kHz) chirp sub-bottom profiler. An example of the plume imaged on one single-beam system is shown in Figure 3. Plume data was extracted by filtering out background water column noise data, based on the simultaneously collected multibeam data, leaving only the acoustic signal associated with the gas venting from the pockmark. Individual acoustic anomalies were removed if they were connected to the seafloor, or single, isolated, and vertically elongated stack of high acoustic energy above noise level. Additionally, the multibeam data allowed us to cross validate the position of plumes and ensure that the relevant target was being examined.

Figure 4 shows examples of the target strength collected by the single-beam systems. Each sonar data set consists of the target strength of the plume at a range of depth in response to frequencies from 3.5 to 200 kHz.

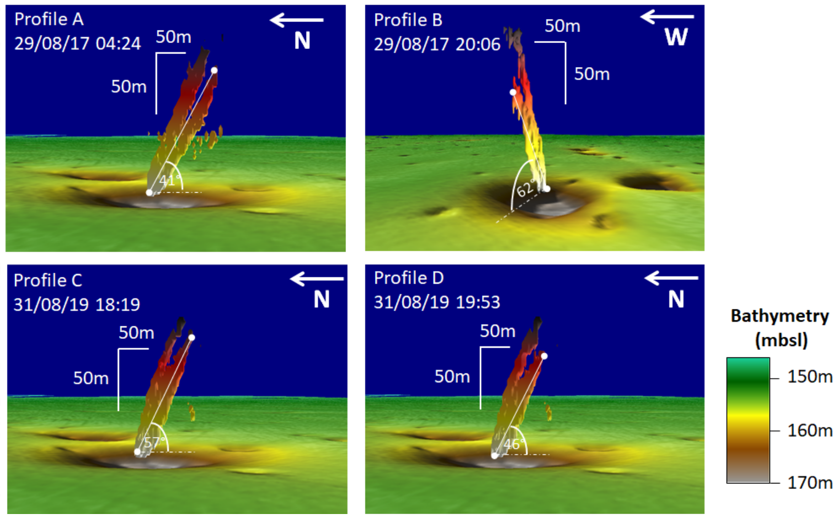

Figure 2: The methane plume at the Western Scanner Pockmark imaged by the EM710 multibeam echo sounder (70-100 kHz) on four multibeam profiles (A-D; position shown in Figure 1). The plume is orientated in the same direction as the tidal flow (i.e. in a North-South direction). The distinct forked shape of the plume can be observed. Plume lateral extent is coloured from white at the base to black at the upper surface.

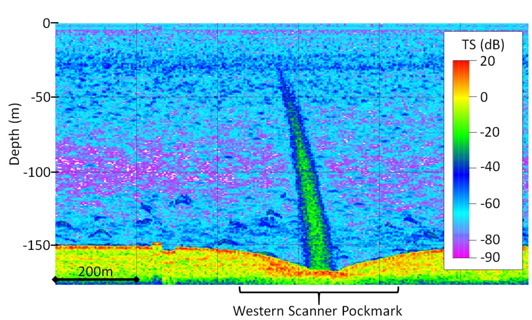

Figure 3: Direct 18 kHz single-beam observation from snap shots of plume for profile C. With the single-beam data we are unable to observe the forking in the multibeam data shown in Figure 2 due to the 2-D profile orientation.

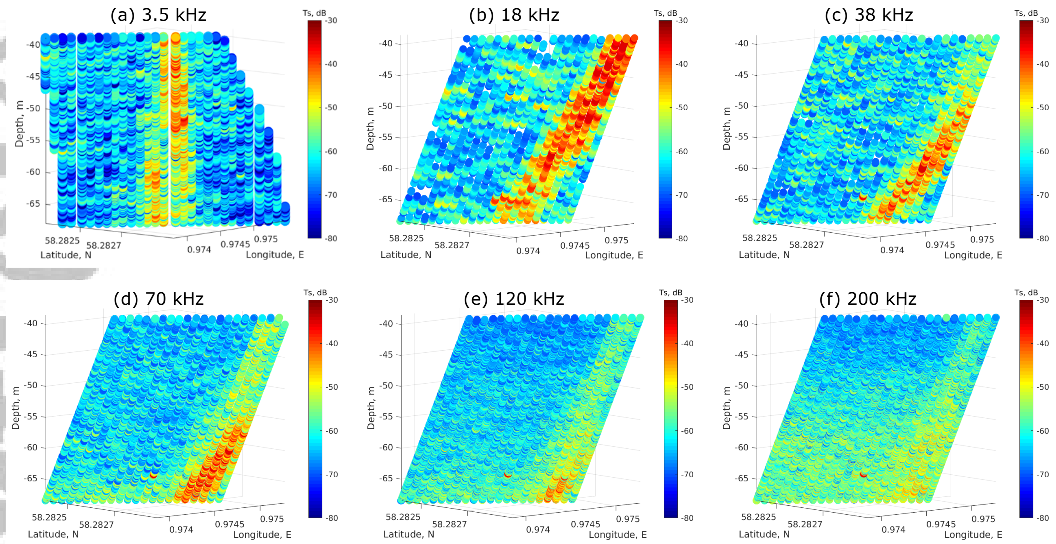

Figure 4: Target strength (Ts) of plume imaged on profile A extracted from single-beam data at each frequency. The target strengths of received signal are between -80 dB and -30 dB. (a) 3.5 kHz; (b) 18 kHz; (c) 38 kHz; (d) 70 kHz; (e) 120 kHz; (f) 200 kHz.

3 Data processing, modelling, and flow rate estimation

This section describes how the observed target strength data is used to determine the depth-dependent bubble size distribution and gas flux of a plume (Figure 5). Acoustic detection and identification of gas plumes can be used to quantify the bubble flow rate if a number of acquisition parameters and assumptions about the physics of methane gas seepage at the seafloor and the surrounding environments are made (Veloso et al., 2015). The multibeam data is used to determine structure of plume arms and the corresponding dimension in depth. The single-beam target strength data is used to derive the observed volume scattering strength in depth. To quantify the bubble size distribution and gas flux, we develop an inversion algorithm which iteratively matches the modelled and measured volume scattering data. For each depth of interest, the shape of the bubble size distribution is parametrized by a log-normal probability density function, with a further parameter defining the total number of bubbles. As mentioned in Section 2, the Scanner Pockmark produces two dominant bubble sizes, and we incorporate this into our model.

3.1 Beam data processing

The intermediate frequencies of each data set are smoothed to create an observation of volume scattering strength as a function of depth and frequency. We denote the received target strength at frequency f of backscattering ping n as $\mathrm{Ts}_n(f)$ [dB], then the volume scattering strength $\mathrm{Vss}_r(f)$ [dB/m^3] can be expressed as (Johanneson & Mitson, 1983)

$$\mathrm{Vss}_r(f) = 10\log_{10}\left(\frac{1}{V}\sum_{n=1}^{N_p} 10^{\mathrm{Ts}_n(f)/10}\right), \tag{1}$$

where N_p is the total number of scatterers in a fragment of volume, and the reverberating volume V is computed as

$$\mathrm{V} = h_i \times S_i, \tag{2}$$

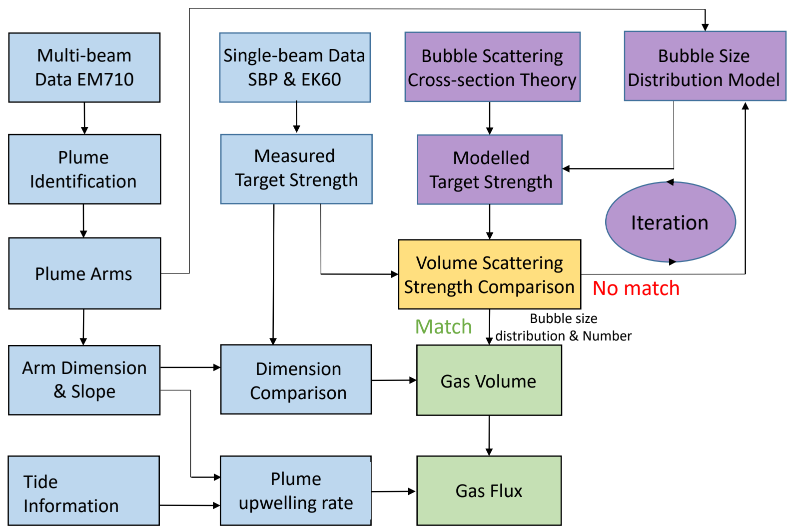

Figure 5: Flow chart describing the processing steps used to determine bubble size and gas flux from the input acoustic data. Blue blocks describe the processing of observed multibeam data, single-beam data, and tidal information; purple blocks describe the iterative volume scattering strength matching model; and green blocks describe the quantification stage.

where h_i is the vertical height and S_i is the scanning area of interest in the horizontal plane. Considering the propagation loss (PL(f)) in the acoustic channel, the volume scattering strength of gas bubbles Vss(f) can be expressed as (Smailes, 1976)

$$\mathrm{Vss}(f) = \mathrm{Vss}_r(f) + \mathrm{PL}(f). \tag{3}$$

Essentially, the PL(f) is the sum of two terms: the geometrical loss ($\mathrm{PL}_g(f)$) and the absorption loss ($\mathrm{PL}_\alpha(f)$) (Li, White, Bull, & Leighton, 2019):

$$\mathrm{PL}(f) = \mathrm{PL}_g(f) + \mathrm{PL}_\alpha(f). \tag{4}$$

Here we assume a spherical spreading model for the geometrical losses, and the absorption loss is calculated from Thorp's formula (J. Urick, 2013; Ochi et al., 2008; Li, White, Bull, & Leighton, 2019; Harris III & Zorzi, 2007). Taking into account the propagation loss, the volume scattering strength of gas bubbles as a function of frequency can be extracted.

3.2 Modelling

The model of the acoustic scattering from the bubble plume combines three basic components: 1) the model of the backscattering cross-section of a single bubble, 2) an assumed shape of the bubble size distribution, and 3) a method to compute the volume scattering strength. Each of these three elements is detailed in a subsequent subsection.

3.2.1 The acoustic backscattering cross-section of a single bubble

The backscattering cross-section of a single bubble is relatively well established when wavelength of the ensonifying sound field is significantly greater than the bubble radius, i.e. $kr \ll 1$ (sometimes referred to as the 'long-wavelength' condition) where k is the wave number equal to $2\pi f/c_w$ with f representing the frequency of the acoustic wave. When using many commercial imaging sonars to examine bubbles from seeps, this condition is frequently violated. For example, for the highest frequency used in this study, 200 kHz, then k is approximately 800 m^{-1}. To keep kr less than 5%, say, in order to make the 'long-wavelength' formulations valid, the seeps should emit no bubbles larger than radius 60 microns for a 200 kHz beam. This maximum allowable bubble size, to keep the 'long-wavelength' formulation valid, decreases with increasing frequency, for example kr = 0.05 for bubbles of 20 micron radius when f = 600 kHz, by no means the highest frequency used to quantify gas from seeps. Given most measurements of seeps show bubble radii that are at least two orders of magnitude larger than this limit then the 'long-wavelength limit' is not justifiable. The gas flux from a seep is dominated by the gas carried in the largest bubbles, so to estimate such fluxes it is most important to accurately model the scattering from these large bubbles. As discussed in Ainslie and Leighton (Ainslie & Leighton, 2009, 2011), when the condition $kr \ll 1$ cannot be relied upon then one needs to take considerable care. In particular, it is necessary to ensure that expressions for the damping terms, arising through three mechanisms: acoustic radiation, viscous and thermal damping, also do not rely upon assuming $kr \ll 1$. Further, the expressions for the cross sections need to be corrected from the prediction of the formulation of the long-wavelength limit (which erroneously predicts that the scattering cross-section increases quadratically with increasing radius). They in fact approximately plateau (onto which resonances are superimposed), which is the prediction from detailed modelling (Thuraisingham, 1997).

The expression we shall consider for the backscattering cross-section, σ_{bs}, is

$$\sigma_{bs}(r,f) = \frac{r^2}{\left(\frac{\omega_0^2}{\omega^2} - 1 - 2\frac{\beta_0}{\omega}kr\right)^2 + \left(2\frac{\beta_0}{\omega} + \frac{\omega_0^2}{\omega^2}kr\right)^2} \frac{\left(\frac{\sin kr}{kr}\right)^2}{1+(kr)^2}, \tag{5}$$

This is adapted from Ainslie and Leighton (Ainslie & Leighton, 2009, 2011) to include the final factor which was proposed by (Thuraisingham, 1997). This expression implicitly includes radiation damping, with the effect of the other two damping mechanisms (viscous and thermal damping) being combined into a single damping factor, β_0. This formulation provides a consistent approach to incorporating radiation damping into the backscattering model, something which as Ainslie and Leighton (Ainslie & Leighton, 2011) showed, cannot be achieved using dimensionless damping coefficient, which is the prevailing approach (Veloso et al., 2015). In (5), the frequency ω_0 is defined through the solution of the equation

$$\omega_0 = \sqrt{\Re\{\Omega^2(r,\omega)\}}, \tag{6}$$

where $\Re\{\cdot\}$ denotes the real part of a complex number. Under specific circumstances (when the process is isothermal or adiabatic) this frequency corresponds to the resonance frequency of the bubble, however, in general this is not the case. The complex parameter Ω, seen in (6), is defined through

$$\Omega^2 = \frac{3}{\rho_{\mathrm{liq}} r^2}\left(\Gamma P_{\mathrm{gas}} - \frac{2\tau}{3r}\right), \tag{7}$$

where ρ_{liq} is the density of the liquid surrounding the bubble [kg/m^3], τ is the surface tension [N/m], and P_{gas} is the pressure of the gas inside the bubble [Pa], which can be expressed as:

$$P_{\mathrm{gas}} = P_{\mathrm{atm}} + \rho_{\mathrm{w}} g d + \frac{2\tau}{r} - p_v, \tag{8}$$

where P_{atm} is the atmospheric pressure [Pa], g is the acceleration due to gravity [m/s^2], p_v is the vapour pressure for water, and d is the depth of the bubble. In (7) Γ represents the complex polytropic index (Ainslie & Leighton, 2011)

$$\Gamma = \frac{\gamma}{1 - \left\{\frac{(1+i)X/2}{\tanh\left((1+i)X/2\right)} - 1\right\}\left(\frac{6i(\gamma-1)}{X^2}\right)}, \tag{9}$$

with γ representing the specific heat ratio, and the parameter X being defined as

$$X = \sqrt{\frac{2\omega}{D_p}}r, \tag{10}$$

and the thermal diffusivity, D_p, of the gas in the bubble can be expressed as

$$D_p = \frac{K_{\text{gas}}}{\rho_{\text{gas}}C_p}, \tag{11}$$

in which the K_{gas} is the thermal conductivity of the gas within the bubble, C_p is the specific heat capacity of the gas at constant pressure. The density of the gas ρ_{gas} can be computed using (Leighton, 1994)

$$\rho_{\text{gas}} = \frac{M_{\text{m}}}{RT}R_{\text{gas}}, \tag{12}$$

where R is the gas constant, and T is the temperature [K] and M_m is the molar mass of the gas.

The two remaining damped effects (thermal and viscous) are included in the model (7) through the combined damping coefficient β_0 defined as

$$\beta_0 = \beta_{\text{th}} + \beta_{\text{vis}}, \tag{13}$$

where β_{th} and β_{vis} are the thermal and viscous damping coefficient [s$^-1$]. Further, expressions for these two quantities can be obtained as (Ainslie & Leighton, 2009, 2011):

$$\beta_{\text{th}} = \frac{\Im\{\Omega^2\}}{2\omega}, \tag{14a}$$

$$\beta_{\text{vis}} = \frac{2\eta_S}{\rho_{\text{liq}}r^2}, \tag{14b}$$

where $\Im\{\cdot\}$ denotes the imaginary part of a complex number, and η_S is the shear viscosity of the liquid [Pa·s]. The form for the viscous damping has been a matter of some discussion, with some authors favouring the inclusion of the effects of bulk viscosity (Love, 1978; Veloso et al., 2015), however, the later analysis of Baik (Baik, 2013) highlighted flaws in the previous work and recommended the use of (14b).

Whilst this model captures much of the physics of acoustic scattering from bubbles in the large wavelength limit it should not be regarded as complete. It still relies on the assumption that the bubbles are spherical, which for large bubbles will not hold true and can affect the backscattering cross-section (Salomatin & Yusupov, 2005; Ostrovsky et al., 2008). Parameters used in the bubble backscattering cross-section computation are summarized in Table 1.

3.2.2 *Bubble size distribution assumption*

To estimate the bubble size distribution for each plume arm, a log-normal distribution (Johnson et al., 1994) is used as an appropriate bubble size distribution to match the plume bubbles (Veloso et al., 2015):

$$p_{\text{b}}(r) = \frac{1}{rS\sqrt{2\pi}}e^{-(\log(r)-\mu)^2/(2S^2)}, \tag{15}$$

Table 1: Parameters used in the cross-section computation

Term	**Notation**	**Value/Unit**
d	water depth	[m]
r	bubble radius	[m]
f	ensonifying frequency	3.5-200 [kHz]
T	measured temperature	8.14 [°C] or 281.29 [Kelvin]
τ	surface tension	0.0745 [N/m]
p_v	vapour pressure	872 [Pa] at 10°C
η_S	shear viscosity	1.5×10^{-3} [P·s]
K_{gas}	thermal conductivity of the gas CH_4	$8{\times}10^{-2}$ [W/(m*k)]
C_{p}	specific heat capacity at constant pressure	2.191 [kJ/(kg K)]
g	gravity	9.81 [m/s^2]
ρ_{liq}	seawater density	1025 [kg/m^3]
P_{atm}	atmospheric pressure	$101{\times}10^3$[Pa]
c_{w}	measured sound speed in water	1485 [m/s]
γ	specific heat ratio of the gas CH_4	1.299
M_{m}	molar mass of the gas CH_4	0.016 [kg/mol]
R	gas constant	8.31 [m^2 kg s^{-2} K^{-1} mol^{-1}]

where

$$\mu = \log(\bar{r}_b) - S^2/2, \tag{16}$$

and

$$S = \sqrt{\log(1 + (\varsigma_b)^2)}. \tag{17}$$

Thus, for each point at which the inversion is applied, we have three parameters to match: the mean radius $\bar{r}_{\mathrm{b}}$ in Eq.(16), the standard deviation ς_{b} in Eq.(17), and the number of bubbles per unit volume N_{b}. The mean radius $\bar{r}_{\mathrm{b}}$ is related to the frequency f_{peak} corresponding to the peak value of the volume scattering strength $\mathrm{Vss}_{\mathrm{peak}}(f)$ for each depth; the deviation ς_{b} is related to the curvature $\mathbf{C}$ of volume target strength curve as a function of frequency f; and the number of bubbles N_{b} is related to the amplitude of the volume scattering strength $\mathbf{Vss}(f)$. The three parameters are initialised at the beginning of the iteration process.

3.2.3 Modelled volume scattering strength

Assuming the backscattering of all bubbles at depth d are uncorrected, the modelled volume scattering strength $\widehat{\mathrm{Vss}}(f)$ [dB] is the sum of the backscattering strength of the individual bubbles in radius bins centred on $[r_1, \ldots, r_{\mathrm{end}}]$, given by

$$\widehat{\mathrm{vss}}(f) = \frac{1}{V} \sum_{r_n = r_1}^{r_{\mathrm{end}}} N_b(r_n)\sigma_{bs}(r_n, f), \tag{18}$$

$$\widehat{\mathrm{Vss}}(f) = 10 \log_{10} \left(\widehat{\mathrm{vss}}(f) \right), \tag{19}$$

where $N_b(r_n)$ is the number of bubbles with radius r_n per unit volume, following the bubble radius probability density function (PDF) $\widehat{p_{\mathrm{b}}}(r)$ in Eq.(15). For a series of frequencies $f = \{f_1, \ldots, f_{\mathrm{end}}\}$, we obtain a vector of $\widehat{\mathbf{Vss}}(f)$.

3.2.4 Linear inversion

One existing approach to quantifying gas from backscattered acoustic signals is based on linear inversion techniques. Such methods have been considered in cases when no bubbles are assumed to be resonant (Nikolovska et al., 2008) and without that restriction (B. Berges, 2015; Muyakshin & Sauter, 2010; Veloso et al., 2015). These methods are based on (19) which can be expressed in matrix form:

$$\mathbf{A}\mathbf{x} = \mathbf{b}, \tag{20}$$

where the elements of the matrix $\mathbf{A}$ are the backscattering strengths, the column vector $\mathbf{x}$ contains the number of bubbles per unit volume within a size bin and $\mathbf{b}$ contains the linear volume scattering strengths. Assuming the matrix $\mathbf{A}$ is of full rank and the number of radius bins is equal to the number of ensonifying frequencies, then this is a square system of equations with a unique solution which can, in principle, be solved through matrix inversion. If the number of radius bins is less than the number of frequencies, a least square solution can be obtained, whilst if the number of radius bins exceeds the number of frequencies the problem is ill-posed and an infinite number of solutions exist.

One problem is that since only a small number of frequencies are typically used to ensonify a cloud, one can only estimate bubbles in a small number of radius bins. Further, the matrix $\mathbf{A}$ can become ill-conditioned as the off-diagonal terms can become large compared to the diagonal elements. This is because both resonant bubbles and large bubbles generate high levels of scattering, so whilst the diagonal elements in $\mathbf{A}$ may be large, so too are the regions corresponding to large bubbles ensonified by high frequencies. This ill-conditioning in $\mathbf{A}$ means that during the inversion process small errors are greatly magnified. This can be mitigated by imposing prior constraints on the problem, in the form of regularisation and by ensuring that the solution is always non-negative.

In this work we eschew the use of linear inversion and at the outset impose constraints on the assumed bubble size distribution, which leads to a non-linear optimisation problem for which cannot be solved within a linear framework.

3.2.5 Matching procedure

Rather than adopting a least squares approach to minimise the difference between the observed and modelled volume scattering strengths we shall use a curve matching strategy. Such an approach allows one to match a curve across the frequency interval at a large number of points, rather than solving the problem at isolated points. There are multiple curve matching techniques that have been proposed, including the Smith-Waterman algorithm for sequence alignment (Gribskov & Robinson, 1996), the B-spline fusion technique (Xia & Liu, 2004), the Discrete Curve Evolution (Bai et al., 2007), and the optimal alignment method (Sebastian et al., 2003). Here we adopt a method based at the optimal alignment curve matching.

The iteration procedure for each plume arm is shown in Appendix A. We first identify the plume arm structure, measure the dimension for each identified arm in depth, compute the observed volume scattering strength $\mathrm{Vss}(f)$ in depth, and prepare coefficients and environmental parameters collected in the experiment as shown in Table 1. For the matching process we must initialise the bubble radius $\bar{r}_b(0)$, the standard deviation $\varsigma_b(0)$, and the total number of bubbles $N_b(0)$. The bubble radius $\bar{r}_b(0)$ is initialised from the plume upwelling velocity v_v as described in Eq.(21); the standard deviation $\varsigma_b(0)$ is initialised as 1 mm; and the total number of bubbles per unit volume is initialised as a positive integer (here we use 100 for the upper arm possessing big bubbles, and 10000 for the lower arm possessing small bubbles). The initial radii, $\bar{r}_b(0)$, is selected to be 0.05 mm and 5 mm, for the lower and upper arms respectively. To accelerate the matching, one may need to adapt these initial values according to the observed target strength as a function of depth and frequency.

For each iteration n of the curve matching method, we calculate the volume scattering strength $\mathbf{Vss}(f)$ as a function of frequency f through Eq.(19). From the calculated $\mathbf{Vss}(f)$ curve, we find frequency of the peak of the curve, $\widehat{f}_{\text{peak}}(n)$, the maximum absolute curvature, $|\widehat{C}_{\max}(n)|$, and the value of the peak volume scattering strength at that point, $\widehat{\mathbf{Vss}}_{\text{peak}}(f,n)$. The magnitude of the difference between the modelled and observed volume scattering strength can be computed, i.e. $\Delta\widehat{\mathbf{Vss}}(f,n) = |\widehat{\mathbf{Vss}}(f,n) - \mathbf{Vss}(f)|$. If the size of this difference is minimized (e.g. on average less than a threshold $\text{Th}_1 = 1$ dB and the largest difference is less than a threshold $\text{Th}_2 = 3$ dB) in a number of iteration steps (e.g. 50), then the iteration is stopped, otherwise, the parameters ($\bar{r}_b$, ς_b, and N_b) are updated according to the recursions shown in Appendix A.

After the iterative matching process, we obtain estimates of the mean radius $\bar{r}_b$, standard deviation ς_b, and the number of bubbles N_b as a function of depth in each of the plume arms. These three parameters define the probability density function (PDF) of the bubble size distribution as a function of depth, so that at any depth one can compute the gas volume and the gas flux.

3.3 Measurement

3.3.1 Measuring plume upwelling velocity

In order to compute the gas flux one need to not only know the amount of gas at a given depth, but also the velocity of the gas. Individual bubbles rise through a liquid as a result of buoyancy, at a rate called the bubble rise velocity. A plume of bubbles also create motion of the surrounding water, creating a circulation (upwelling), this is the plume upwelling velocity and represents the velocity of bubbles in the plume, which is required in the flux calculation.

To estimate the plume upwelling velocity, we use the plume slope angle and modelled sea current speed. The average slope l_{p} (highlighted in Figure 2), is obtained by measuring the height and extent of the plume. The slope of the plume varies with depth, tide and current (Sündermann & Pohlmann, 2011). However, our multibeam data (Figure 2) suggests that the plumes observed here rise at an approximately constant angle and we use that angle to estimate a constant plume upwelling velocity.

We assume that the horizontal displacement of plume is entirely controlled by the current. Thus we assume the relationship/slope angle θ between the horizontal displacement X_h and vertical displacement X_v of the plume is equal relationship between the horizontal velocity v_h (the current) and the plume upwelling velocity v_v. The plume slope is then given by:

$$l_p = \frac{X_v}{X_h} = \tan\theta = \frac{v_v}{v_h}. \tag{21}$$

Using (21) the average plume upwelling velocity near the pockmark values ranging from 10 to 15 cm/s. These values correspond to the bubble rise velocities for bubbles with radii in the range 1−6 mm (Park et al., 2017). This is consistent with our choice of an initial mean bubble radius in the upper arm.

3.3.2 Gas volume estimation

The plume is assumed to have an ellipsoidal cross-section in the horizontal plane as observed from the multibeam data (Figure 2). The major and minor axes of the ellipse are denoted D_l and D_s which can be measured from the 3-D multibeam data. We consider the gas in the plume in terms of horizontal slices of constant height (here we use 1 m). The scattered signal measured at the single-beam echo-sounder consists of contributions from a volume which is approximately cylindrically shaped oriented along the axis of the beam shown. The length of the cylinder being $c_{\text{w}}\tau/2$ (where τ is the pulse

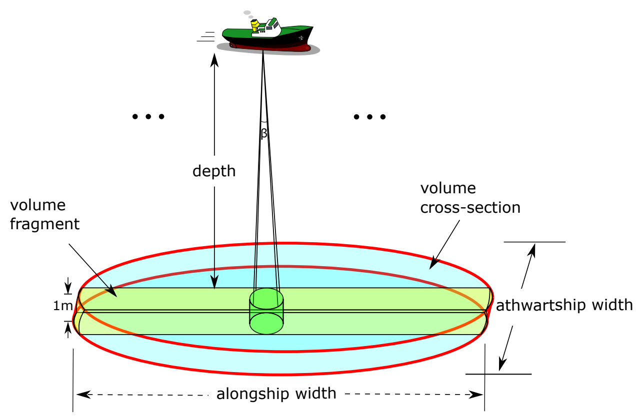

Figure 6: Geometry for converting gas volume from reverberating volume area to plume volume in depth. The single-beam scanned area is a fragment of the plume cross-section. The plume horizontal cross-section is considered to ellipse as observed from the multibeam data shown in Figure 2. Note that the alongship width and athwartship width are function of the longest diameter and shortest diameter of the ellipse relying on the ship direction.

duration) and the diameter of the cylinder is $2h\tan(\beta/2)$, where h is the depth and β is the beamwidth (Figure 6). Assuming a horizontal cross-section of the plume is homogeneous, having the same properties as the observed beam fragment, we can multiple our findings appropriately to represent the whole horizontal cross-section of the plume.

Based on the estimated bubble size distribution the gas volume $\widehat{\mathrm{V}}_p$ [L] within 1 m thick section through the plume can be approximated using

$$\widehat{\mathrm{V}}_p = \sum_{bin=1}^{Bin} \frac{4}{3}\pi N(r_{bin}) r_{bin}^3. \tag{22}$$

Figure 6 shows the geometry for converting gas volume from reverberating volume area to plume volume in depth. The calculated gas volumes are only a fragment of the gas volume in the whole gas plume arm at their corresponding depth (or horizontal cross-section). We measure the size of the horizontal area in the reverberating volume fragment V according to the beamwidth. With the measured plume dimension S_h, and the gas volumes for each fragment $\widehat{\mathrm{V}}_p$, we calculate the gas volume $\widehat{\mathrm{V}}_h$ for each horizontal cross-section at each depth with $\mathrm{h}_v = 1$ m thickness:

$$\widehat{\mathrm{V}}_h = \frac{\mathrm{S}_h}{\mathrm{S}_p}\widehat{\mathrm{V}}_p, \tag{23}$$

where S_p is the horizontal dimension of the volume fragment.

3.3.3 Gas flux determination

Because of the interaction between the plume arms and the sea current, the rise velocity of the small bubbles in the lower plume arm is forced to be similar to that of upper plume arm containing larger bubbles. The mean rise velocity of the bubbles in the upper sub-plume are calculated using Eq.(21). The estimated plume gas volumes $\mathrm{V_g}$ and the bubble rise velocity, we obtain the gas fluxes $\hat{\mathrm{F}}_g$ [L/min] of the upper plume arm and the lower plume arm in depth:

$$\widehat{\mathrm{F}}_g = \widehat{\mathrm{V}}_h v_v/\mathrm{h}_v, \tag{24}$$

where h_v is the volume thickness, which here is equal to 1 m, considering the pulse length and resolution.

4 Results

Primary observations of this data set (Figure 7) show strong volume scattering strength at 3.5-18 kHz and 70-120 kHz. For larger bubbles that rise faster than smaller bubbles (due to increased buoyancy), the movement direction of bubbles is closer to vertical. The target strength of the plume is integrated as volume scattering strength in depth for 1 m thickness and smoothed as shown in Figure 7. Two bubble clouds are visible, one in 3.5-18 kHz and the other in 38-200 kHz, and with a somewhat blurred border between them. At the low frequencies ($f < 18$ kHz), the clouds are connected to each other without big gaps, while at high frequencies ($f > 38$ kHz), the clouds are more separated from each other compared to those at low frequencies. This is consistent with arm structures observed from the multibeam observations, with small bubbles (radii < 0.2 mm) producing the peak at around 120 kHz and large bubbles (radii > 0.2 mm) producing the peak at much lower frequencies (Figure 7 left column).

Using the model matching approach, Section 3.2.5, we obtained the scattering profiles shown in Figure 7 middle column. This process also yields estimates of the parameters defining the bubble size distribution as a function of depth. The difference between the modelled and observed volume scattering strength is shown in Figure 7 right column. For all these cases, we successfully matched the scattering strength with only small difference remaining. This process also yields estimates of the parameters defining the bubble size distribution as a function of depth. To verify the gas flux change in depth, we compare the results to the predictions from a numerical model, specifically the Methane Individual Bubble Impact (MIBI) model (Dewar, 2016).

4.1 Plume structure identification

The two-arm structure that we observe for the plume is consistent with that presented in the literature (McGinnis et al., 2006; Gentz et al., 2014; von Deimling et al., 2015; Leifer et al., 2017; Sommer et al., 2015; Ruppel, 2011; Dissanayake et al., 2018; Greinert et al., 2006). It is proposed that the observed plume structure is a consequence of two dominant peaks in the bubble size distribution. The plume was observed multiple times from different directions, and the two-arm structure is consistently observed (see Figure 2). Acoustic data available for volume scattering strength analysis are at water depths 39-73 m and 86-145 m (Figure 7).

4.2 Bubble size distribution

Identifying the structure of plume is one of the important elements in quantifying gas flow rate. Another important issue is related to bubble size distribution of each plume arm. Here, we determine the bubble size distribution using the iterative volume scattering strength matching model. Applying the model yields two different bubble size distributions for the two plume arms. The acoustic measurements at two bathymetric depths result in similar bubble size distributions.

Figure 8(a) shows the PDF of the upper and lower plume arms at depth 65 m and 145 m, respectively. From the estimation, bubbles in the upper arm possess radii mainly between 1 mm and 15 mm, while bubbles in the lower arm possess radii mainly between 0.01 mm and 0.15 mm. In the upper arm, there are more bubbles at 145 m than that at 65 m at all radii. In the lower arm, there are more relatively large bubbles (0.025-0.15 mm) at 145 m than that at 65 m, while there are fewer relatively small bubbles (< 0.025 mm) at 145 m than that at 65 m. In the upper arm, the mean radius of the bubbles is $\bar{r}_b =$ 5 mm, and the bubble size distributions are comparable with those estimated elsewhere in the literature (1 mm to 6 mm) (Greinert, McGinnis, et al., 2010; Leifer & Patro, 2002; Muyakshin & Sauter, 2010; Ostrovsky et al., 2008; Römer et al., 2011; Sahling et al., 2009; Veloso et al., 2015).

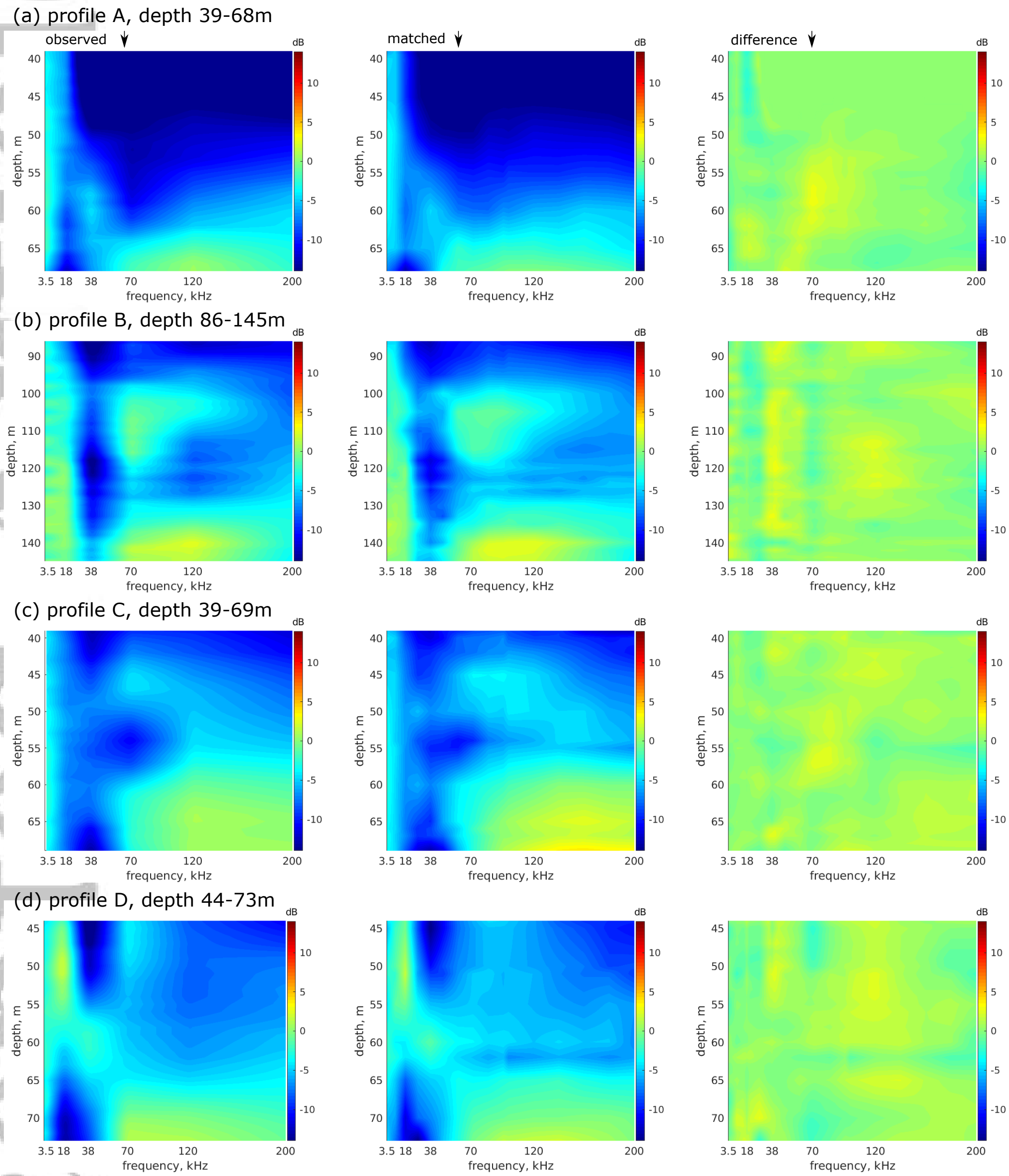

Figure 7: Left column: observed volume scattering strength of gas bubbles as a function of depth and frequency for the four profiles across the Scanner Pockmark methane. Data input was the volume scattering strengths observed at frequencies of 3.5, 18, 38, 70, 120 and 200 kHz; intermediate values are smoothed from the available data. Middle column: matched volume scattering strength as a function of depth and frequency for the four profiles. Right column: difference between the matched and the observed volume scattering strength as a function of depth and frequency for the four profiles. After sufficient iterations, the mean and maximum differences between the matched and observed volume scattering strength for most of these profiles are limited in 1 dB and 3 dB, respectively.

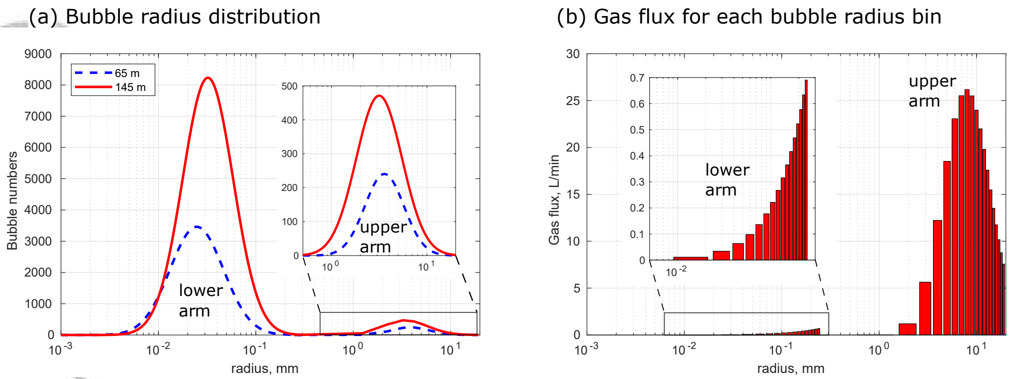

Figure 8: (a) Bubble radius distribution estimated from volume scattering strength matching at depths of 65 m and 145 m, respectively. In the upper arm, bubble radii are predominantly in the interval [1 mm, 15 mm]; in the lower arm, bubble radii are predominantly in the interval [0.01 mm, 0.15 mm]. (b) Relative gas flux comparison for each bubble radius bin at depth 145 m. The highest gas flux is contributed by bubbles with radii of about 8 mm.

4.3 Gas flow rate quantification

The Scanner Pockmark plume was imaged on multiple profiles in different directions and the volume extent of methane bubbles in the water column is well constrained by multibeam data. Using the water column volume mapped from the multibeam data, we could extrapolate the volume scattering strength derived measurements from single-beam data from the four profiles. We accept that our transect-derived estimates of bubble density and distribution may be a simplification of the 3-D plume.

With the measured sizes and the maximum gas volumes for each fragment, we calculate the gas volumes $\widehat{\mathrm{V}}_{\mathrm{h}}$ for each horizontal cross-section at 1 m intervals in depth. With the estimated plume gas volumes, we obtain the dominant gas fluxes of both the upper and lower plume arms (Figure 9). From the calculation of gas flux for each size interval of bubbles, we obtain the relative gas flux contribution for each bubble size interval. It shows that the highest contribution of gas flux is from bubbles at radii of about 8 mm, and the contribution of gas flux from the lower plume arm can be omitted as shown in Figure 8(b).

The results described in Figure 9 allow the estimation of *in situ* instantaneous flow rates in the water column, and for the upper plume this is 1.56×10^6 kg/year (294 L/min) at 145 m water depth, while for the same depth, the lower arm flow rate is 2.6×10^4 kg/year (4.9 L/min). In this form of depth-based estimation, the upper arm contributes 98% to the gas emission, whereas 2% are from the bubbles in the lower plume. The gas flux determination results suggest that the upper arm with large bubbles dominates the gas flux of the seabed released methane from the Scanner Pockmark. In addition to the flow rate estimates close to the pockmark, we also estimate gas flow rate in the water column associated with four different tidal heights. While at different tidal heights, comparing that of profiles A (0.4 m) and C (0.2 m) for example, the variation of gas flux can be up to 40 L/min (2.4×10^5 kg/year at depth 165 m in the upper arm (Figure 9(a)) and can be up to 1.0 L/min (6.0×10^3 kg/year at depth 165 m in the lower arm (Figure 9(b)).

The gas flux gradually decreases from 1.56×10^6 kg/year (294 L/min) at depth 145 m to 6.9×10^4 kg/year (40 L/min) in the upper arm at depth 40 m as a consequence of bubble dissolution. In the lower arm, no obvious trend in gas flow rate is visible due to the intermittent emission of smaller bubbles. Overall, for the western Scanner Pockmark plume,

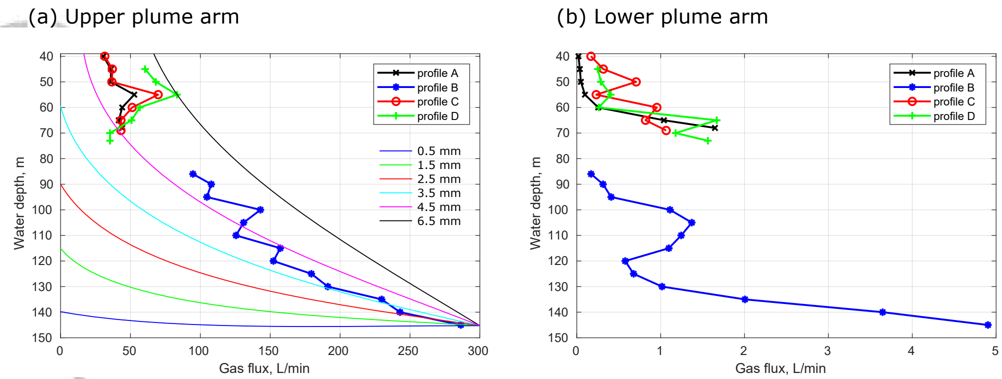

Figure 9: Estimated gas flux for each plume arm. (a) upper plume arm; lines with markers on are measured gas flux for each profile; lines without markers on are from the MIBI modelling (Dewar, 2016) of the methane bubbles, which match the measured gas flux quite well in depth; 0.5-6.5 mm are bubble radius. (b) lower plume arm.

the instantaneous flow rate is estimated to 1.59×10^6 kg/year (299 L/min) at depth 145 m, and 2.4×10^6 kg/year (400 L/min) at depth 165 m extrapolating the results in Figure 9 downwards to the base of the pockmark. This instantaneous value may not be wholly representative of average flow rate, as in this study we have not considered tidal or seasonal variability.

4.4 Gas flux verification of upwelling methane plume using modelling

To verify the gas flux evolution along the plume, we apply modelling of the methane bubbles known as the MIBI model (Dewar, 2016). This is a modified version of a CO_2 bubble model developed by Chen et al. (Chen et al., 2009), recreated in a study to compare impacts of CO_2 and methane in the water column (Dewar et al., 2013). To simulate methane, the dominant gas properties on the bubble dynamics and dissolution have been used.

The results obtained from the MIBI model, are shown as lines in Figure 9(a). The model suggests that the dominant bubble radii is somewhere around 4.5 mm (between 3.5 and 6.5 mm), as superimposed for comparison in Figure 9(a). This size best matches the measurements made from Profile B. The dominant bubble radius in the plume appears to be around the 4.5-5 mm mark, this is slightly larger than the measured peak bubble radius of 3.5 mm. However, this is to be expected given that bubbles of radii up to 20 mm are measured in the plume. The MIBI model also predicts that the reduction in plume volume from dissolution and the bubble expansion from reduced pressure. The results at bubble radius between 4.5 and 6.5 mm match well with the acoustic measurements at profiles A, C, and D, validating the effectiveness of our approach.

5 Uncertainty estimation and discussion

To remove ambiguities, one must use frequencies both above and below those of the bubble resonances present. Most multibeam echosounders have frequencies which, unless one is looking at very deep seeps, are mostly higher than the bubble resonances present. To remove all ambiguities, the lowest frequency used must be lower than the resonance of the largest bubble present (calculated above to be around 1 kHz). With the smallest bubbles presented calculated to have a resonance of 12 kHz, then with the energy available in this experiment from 2.5-6.5 kHz from the chirp, and 18 kHz from the

Table 2: Measured and applied parameters in the estimation approach.

terms	unit	applied	minimum	maximum
temperature	°C	8.1	7.6	10.1
salinity	g/kg	35.1	35.0	35.2
sound speed in water	m/s	1485	1483	1489
density	kg/l	1028.0	1027.5	1028.5
damping coefficient	clean/dirty bubbles	clean	clean	dirty
plume slope (e.g.)	degree (°)	44.5	41.0	48.0

echosounder, we have obtained energy that is at frequencies that are less than the resonances of most of the bubbles present, but not below that of the largest bubbles present. This is an improvement, but does not reach the ideal of achieving a stiffness-controlled scattering from the largest bubbles present (Leighton, 1994).

When considering uncertainty in our calculation of total gas flux, we need to consider two components: the errors due to uncertainty in individual parameters which are inputs into our calculation; and the propagation of this uncertainty in the model. We initially describe errors in individual parameters, before utilising a Monte Carlo simulation approach to understand the uncertainty in the calculation of total gas flux. The Monte Carlo simulations are based on 1000 repetitions, we define measures of uncertainty in the flow rate empirically for the pockmark by varying only one input parameter at a time, holding all others at constant values.

Table 2 describes the uncertainty in physical model parameters in the model. While the uncertainty in some physical parameters are small (e.g. temperature, sound speed in water, salinity) and not significant, others are much larger. We focus here on discussion of those parameters that have significant uncertainty. The overall uncertainty of the flow rate estimation based on the applied physics is defined as a simple superposition (multiplication) of individual factors of uncertainty as follows. The temperature that we are using in the model is an averaged one of 8.1°C (or 281.25 K) in a range of measured temperature [7.6°C, 10.1°C] (or [280.75 K, 283.25 K]). The sound speed in the seawater was measured as between 1483 m/s and 1489 m/s with an average of 1485 m/s. For the shallow water scenario, we choose to calculate clean bubbles as we assume that gas hydrates are stable (Leifer et al., 2000). However, this clean bubble assumption in shallow water may not hold in all cases, thus we include the dirty bubbles in the uncertainty estimation. Application of sea current and plume slope to determine plume upwelling velocity (then bubble rise velocity) remains a variation factor of 8% relative to the seabed. The matching difference between the modelled and observed volume scattering strength is limited within a threshold of 1 dB.

After the Monte Carlo simulation, we obtain the uncertainty of gas flow rate as follows. The temperature affects the viscosity and results in -2% to 0.4% uncertainty of the cross-section computation, with lower temperatures generally reducing the flow rate. The sound speed affects the wave number k and re-radiation damping coefficient δ_{rad}, and can result in -0.4% to 0.3% uncertainty. Such uncertainty resulted from seafloor temperature, near seafloor salinity, sound speed, and seawater density in the shallow water shelf environments, and impact on flow rate estimation was found to be nearly indiscernible. While the dirty bubble assumption reduces the flow rate and results in -21% lower gas flux estimation than that of the clean bubble assumption. The plume slope makes -11.5% to 12% uncertainty of plume upwelling velocity values, then the flow rate. A measure-

Table 3: Uncertainty estimation of gas flux $\widehat{\mathrm{F}}_g$ [L/min] using Monte Carlo approach.

terms	**minimum** $\widehat{\mathbf{F}}_g$	**maximum** $\widehat{\mathbf{F}}_g$	**uncertainty**
temperature	897	919	[-2.0%, 0.4%]
sound speed in water	911	918	[-0.4%, 0.3%]
damping coefficient	723	915	[-21.0%, 0.0%]
plume slope	810	1034	[-11.5%, 13.0%]
Total			[-32%, 14%]

Table 4: Notation used in the text

n	number of iterations
$\bar{r}_b$	bubble mean radius
ς_b	standard deviation of the bubble radius
N_b	total number of bubbles
$\mathbf{Vss}(f)$	observed volume scattering strength in the function of frequency f
$\mathbf{Vss}_{\mathrm{peak}}(f)$	peak value of observed volume scattering strength
$\lvert\mathbf{C}_{\mathrm{peak}}\rvert$	maximum absolute value of curvature of observed volume scattering strength curve
f_{peak}	frequency corresponding to peak value of observed volume scattering strength
$\widehat{\mathbf{Vss}}$	modelled target strength in the function of frequency f
$\widehat{\mathbf{Vss}}_{\mathrm{peak}}$	peak value of modelled volume scattering strength
$\lvert\widehat{\mathbf{C}}_{\mathrm{peak}}\rvert$	maximum absolute value of curvature of modelled volume scattering strength curve
$\widehat{f}_{\mathrm{peak}}$	frequency corresponding to peak value of modelled volume scattering strength
$\Delta\widehat{\mathbf{Vss}}$	difference between observed and modelled volume scattering strength
$\Delta\widehat{\mathbf{Vss}}_{\mathrm{mean}}$	mean value of the volume scattering strength difference
$\Delta\widehat{\mathbf{Vss}}_{\mathrm{max}}$	maximum value of the volume scattering strength difference
$\widehat{V}_p$	estimated gas volume of observed fragment
$\widehat{V}_h$	estimated gas volume of an entire horizontal cross-section with 1 m thickness
$\widehat{F}_g$	estimated gas flux

ment of the overall uncertainty in the calculations can be defined by combining statistics of the range in estimated flow rate values and uncertainty from the theory of flow rate estimation. Totally, the cumulative uncertainty bounds on the average reported flow rates are -32% to 14%. We outline in the following our approach to define an overall uncertainty in the reported values of flow rates, summarized in Table 3.

Our estimated total instantaneous flow rates of 2.4×10^6 kg/year is a representative first-order value for the gas flow at the Scanner Pockmark in the central North Sea, and we propose a total uncertainty in the flow rate estimation of [-32%, 14%]. However, if one assumes in the scattering model that $kr \ll 1$ (Thuraisingham, 1997; Veloso et al., 2015) then one estimates the flux as 1.3×10^6 kg/year and using the new model described here (Section 3.2.1) that estimate becomes 2.4×10^6 kg/year.

6 Conclusions and discussion

In this paper, we developed a new methodology for calculating gas flux from a seabed seep using multibeam imaging, and quantification from single-beam echosounders covering a broad bandwidth (3.5-200 kHz). We investigate a methane seep from the Scanner Pockmark in the North Sea and find that the plume in the water column is forked with two arms. The broadband methodology enables us to quantify gas flux with frequencies spanning the resonances of all the bubbles in the plume. It applies an iterative model to match the volume scattering strength from the water column for each of the plume arm. The matching results show that the upper arm comprises larger bubbles (1-15 mm in radius) and the lower arm comprises smaller bubbles (0.01-0.15 mm in radius). The total seabed methane gas flux is quantified to be between 1.6 and 2.7×10^{6} kg/year (272 to 456 L/min) at the Scanner Pockmark.

Appendix A Volume Scattering Strength Matching Algorithm

Algorithm 1 Volume Scattering Strength Matching Model for each depth of a single plume arm

Require: plume arm structure, arm dimensions in depth, Volume scattering strength $\mathbf{Vss}(f)$ in the function of frequency f for each depth, coefficients and environmental parameters shown in Table 1

Ensure: $\bar{r}_b(0)$, $\varsigma_b(0)$, $N_b(0)$; **pre-decision**: $\bar{r}_b(1)=\bar{r}_b(0)/2$, $\bar{r}_b(2)=2\bar{r}_b(0)$; $\varsigma_b(1)=\varsigma_b(0)/2$, $\varsigma_b(2)=2\varsigma_b(0)$; $N_b(1)=N_b(0)/2$, $N_b(2)=2N_b(0)$

procedure
    for n = 3, … **do**
        if $\widehat{f}_{\text{peak}}(n) \geq f_{\text{peak}}$ **then**
            update $\bar{r}_b(n) \leftarrow (\bar{r}_b(n-1) + \max(\bar{r}_b(n-2), \bar{r}_b(n-3)))/2$
        else
            update $\bar{r}_b(n) \leftarrow (\bar{r}_b(n-1) + \min(\bar{r}_b(n-2), \bar{r}_b(n-3)))/2$
        end if
        if $|\widehat{C}_{\max}(n)| \geq |C_{\max}|$ **then**
            update $\varsigma_b(n) \leftarrow (\varsigma_b(n-1) + \max(\varsigma_b(n-2), \varsigma_b(n-3)))/2$
        else
            update $\varsigma_b(n) \leftarrow (\varsigma_b(n-1) + \min(\varsigma_b(n-2), \varsigma_b(n-3)))/2$
        end if
        if $\widehat{\mathbf{Vss}}_{\text{peak}}(f,n) \geq \mathbf{Vss}_{\text{peak}}(f)$ **then**
            update $N_b(n) \leftarrow N_b(n-1)/\max\left(\mathbf{vss}_{\text{peak}}(f)/\widehat{\mathbf{vss}}_{\text{peak}}(f,n)\right)$
        else
            update $N_b(n) \leftarrow N_b(n-1) * \max\left(\mathbf{vss}_{\text{peak}}(f)/\widehat{\mathbf{vss}}_{\text{peak}}(f,n)\right)$
        end if
    end for
end procedure
update the modelled volume scattering strength $\widehat{\mathbf{Vss}}(n)$ in Eq.(19)
calculate $\Delta\widehat{\mathbf{Vss}}(f,n) = \widehat{\mathbf{Vss}}(f,n) - \mathbf{Vss}(f)$
if $\Delta\widehat{\mathbf{Vss}}_{\text{mean}}(f,n) < \text{Th}_1$ (e.g. 1 dB) & $\Delta\widehat{\mathbf{Vss}}_{\max}(f,n) < \text{Th}_2$ (e.g. 3 dB) **then**
    save $\bar{r}_b(n)$, $\varsigma_b(n)$, $N_b(n)$.
end if
Output : $\widehat{\text{V}}_p$, $\widehat{\text{V}}_h$, $\widehat{\text{F}}_g$ calculation in Eqs.(22),(23),(24).

Acknowledgments

Funding for this work was provided by NERC grant NE/N01610/1 and the European Unions Horizon 2020 research and innovation programme under the grant agreement number 654462 (STEMM-CCS). We are grateful to the Captain of the RRS James Cook and crew for enabling the scientific measurements at sea during JC152.

Data supporting this study (https://doi.org/10.5258/SOTON/D1357) is openly available from the University of Southampton repository.

References

Ainslie, M. A., & Leighton, T. G. (2009). Near resonant bubble acoustic cross-section corrections, including examples from oceanography, volcanology, and biomedical ultrasound. *The Journal of the Acoustical Society of America*, *126*(5), 2163–2175. doi: 10.1121/1.3180130

Ainslie, M. A., & Leighton, T. G. (2011). Review of scattering and extinction cross-sections, damping factors, and resonance frequencies of a spherical gas bubble. *The Journal of the Acoustical Society of America*, *130*(5), 3184–3208. doi: 10.1121/1.3628321

Bai, X., Latecki, L. J., & Liu, W.-Y. (2007). Skeleton pruning by contour partitioning with discrete curve evolution. *IEEE Transactions on Pattern Analysis and Machine Intelligence*, *29*(3), 449–462. doi: 10.1109/TPAMI.2007.59

Baik, K. (2013). Comment on Resonant acoustic scattering by swimbladder-bearing fish[J. Acoust. Soc. Am. 64, 571–580 (1978)](L). *The Journal of the Acoustical Society of America*, *133*(1), 5–8. doi: 10.1121/1.4770261

Baik, K., Leighton, T. G., & Jiang, J. (2014). Investigation of a method for real time quantification of gas bubbles in pipelines. *The Journal of the Acoustical Society of America*, *136*(2), 502–513. doi: 10.1121/1.4881922

Bayrakci, G., Scalabrin, C., Dupré, S., Leblond, I., Tary, J.-B., Lanteri, N., … others (2014). Acoustic monitoring of gas emissions from the seafloor. Part II: a case study from the Sea of Marmara. *Marine Geophysical Research*, *35*(3), 211–229. doi: 10.1007/s11001-014-9227-7

Berges, B. (2015). *Acoustic detection of seabed gas leaks, with application to Carbon Capture and Storage (CCS), and leak prevention for the oil and gas industry* (PhD dissertation). University of Southampton.

Berges, B. J., Leighton, T. G., & White, P. R. (2015). Passive acoustic quantification of gas fluxes during controlled gas release experiments. *International Journal of Greenhouse Gas Control*, *38*, 64–79.

Blackford, J., Stahl, H., Bull, J. M., Berges, B. J., Cevatoglu, M., Lichtschlag, A., … others (2014). Detection and impacts of leakage from sub-seafloor deep geological carbon dioxide storage. *Nature Climate Change*, *4*(11), 1011. doi: 10.1038/nclimate2381

Cazenave, P. W., Torres, R., & Allen, J. I. (2016). Unstructured grid modelling of offshore wind farm impacts on seasonally stratified shelf seas. *Progress in Oceanography*, *145*, 25–41. doi: 10.1016/j.pocean.2016.04.004

Chen, B., Nishio, M., Song, Y., & Akai, M. (2009). The fate of CO_2 bubble leaked from seabed. *Energy Procedia*, *1*(1), 4969–4976. doi: 10.1016/j.egypro.2009.02.329

Dewar, M. (2016). *Modelling the two-phase plume dynamics of CO_2 leakage into open shallow waters* (PhD dissertation). Heriot-Watt University.

Dewar, M., Wei, W., Khajepor, S., McNeil, D., & Chen, B. (2013). Comparison of the impact and fate of leaked CO_2 and CH_4 bubbles from the seabed on the near field waters within the North Sea. In *Egu general assembly conference abstracts* (Vol. 15).

Dissanayake, A. L., Gros, J., & Socolofsky, S. A. (2018). Integral models for bubble, droplet, and multiphase plume dynamics in stratification and crossflow. *Envi-*

ronmental Fluid Mechanics, *18*(5), 1167–1202. doi: 10.1007/s10652-018-9591-y

Gentz, T., Damm, E., von Deimling, J. S., Mau, S., McGinnis, D. F., & Schlüter, M. (2014). A water column study of methane around gas flares located at the West Spitsbergen continental margin. *Continental Shelf Research*, *72*, 107–118. doi: 10.1016/j.csr.2013.07.013

Greinert, J., Artemov, Y., Egorov, V., De Batist, M., & McGinnis, D. (2006). 1300-m-high rising bubbles from mud volcanoes at 2080 m in the Black Sea: Hydroacoustic characteristics and temporal variability. *Earth and Planetary Science Letters*, *244*(1-2), 1–15. doi: 10.1016/j.epsl.2006.02.011

Greinert, J., Lewis, K., Bialas, J., Pecher, I. A., Rowden, A., Bowden, D., . . . Linke, P. (2010). Methane seepage along the Hikurangi Margin, New Zealand: Overview of studies in 2006 and 2007 and new evidence from visual, bathymetric and hydroacoustic investigations. *Marine Geology*, *272*(1-4), 6–25. doi: 10.1016/j.margeo.2010.01.017

Greinert, J., McGinnis, D. F., Naudts, L., Linke, P., & De Batist, M. (2010). Atmospheric methane flux from bubbling seeps: Spatially extrapolated quantification from a Black Sea shelf area. *Journal of Geophysical Research: Oceans*, *115*(C1). doi: 10.1029/2009JC005381

Greinert, J., & Nützel, B. (2004). Hydroacoustic experiments to establish a method for the determination of methane bubble fluxes at cold seeps. *Geo-Marine Letters*, *24*(2), 75–85. doi: 10.1007/s00367-003-0165-7

Gribskov, M., & Robinson, N. L. (1996). Use of receiver operating characteristic (ROC) analysis to evaluate sequence matching. *Computers & chemistry*, *20*(1), 25–33. doi: 10.1016/S0097-8485(96)80004-0

Harris III, A. F., & Zorzi, M. (2007). Modeling the underwater acoustic channel in ns2. In *Proceedings of the 2nd international conference on Performance evaluation methodologies and tools* (p. 18). doi: 10.1145/1345263.1345286

Johanneson, K., & Mitson, R. (1983). Fisheries acoustics. A practical manual for aquatic biomass estimation. *FAO Fish. Tech. Pap*, *240*, 99-101.

Johnson, N. L., Kotz, S., & Balakrishnan, N. (1994). Continuous univariate distributions, vol. 1.

J. Urick, R. (2013). *Principles of Underwater Sound (4th edition).* PENINSULA PUBLISHING.

Kennett, J. P., Cannariato, K. G., Hendy, I. L., & Behl, R. J. (2003). Methane hydrates in quaternary climate change: the clathrate gun hypothesi. *Methane Hydrates in Quaternary Climate Change: The Clathrate Gun Hypothesis*, *54*, 1–9. doi: 10.1002/9781118665138.ch0

Leblond, I., Scalabrin, C., & Berger, L. (2014). Acoustic monitoring of gas emissions from the seafloor. Part I: quantifying the volumetric flow of bubbles. *Marine Geophysical Research*, *35*(3), 191–210. doi: 10.1007/s11001-014-9223-y

Leifer, I., & Boles, J. (2005). Measurement of marine hydrocarbon seep flow through fractured rock and unconsolidated sediment. *Marine and Petroleum Geology*, *22*(4), 551–568. doi: 10.1016/j.marpetgeo.2004.10.026

Leifer, I., Chernykh, D., Shakhova, N., & Semiletov, I. (2017). Sonar gas flux estimation by bubble insonification: application to methane bubble flux from seep areas in the outer Laptev Sea. *The Cryosphere*, *11*(3), 1333–1350. doi: 10.5194/tc-11-1333-2017

Leifer, I., & Patro, R. K. (2002). The bubble mechanism for methane transport from the shallow sea bed to the surface: A review and sensitivity study. *Continental Shelf Research*, *22*(16), 2409–2428. doi: 10.1016/S0278-4343(02)00065-1

Leifer, I., Patro, R. K., & Bowyer, P. (2000). A study on the temperature variation of rise velocity for large clean bubbles. *Journal of Atmospheric and Oceanic Technology*, *17*(10), 1392–1402. doi: 10.1175/1520-0426(2000)017⟨1392:ASOTTV⟩2.0.CO;2

Leighton, T. G. (1994). *The acoustic bubble*. Academic press.

Leighton, T. G., Baik, K., & Jiang, J. (2012). The use of acoustic inversion to estimate the bubble size distribution in pipelines. *Proceedings of the Royal Society A: Mathematical, Physical and Engineering Sciences*, *468*(2145), 2461–2484. doi: 10.1098/rspa.2012.0053

Leighton, T. G., Meers, S. D., & White, P. R. (2004). Propagation through nonlinear time-dependent bubble clouds and the estimation of bubble populations from measured acoustic characteristics. *Proceedings of the Royal Society of London. Series A: Mathematical, Physical and Engineering Sciences*, *460*(2049), 2521–2550. doi: 10.1098/rspa.2004.1298

Leighton, T. G., Phelps, A. D., Ramble, D. G., & Sharpe, D. A. (1996). Comparison of the abilities of eight acoustic techniques to detect and size a single bubble. *Ultrasonics*, *34*(6), 661–667. doi: 10.1016/0041-624X(96)00053-4

Leighton, T. G., & White, P. R. (2011). Quantification of undersea gas leaks from carbon capture and storage facilities, from pipelines and from methane seeps, by their acoustic emissions. *Proceedings of the Royal Society A: Mathematical, Physical and Engineering Sciences*, *468*(2138), 485–510. doi: 10.1098/rspa.2011.0221

Li, J., Roche, B., Bull, J. M., White, P. R., Davis, J. W., Deponte, M., ... Cotterle, D. (2020). Passive acoustic monitoring of a natural CO_2 seep site - implications for Carbon Capture and Storage. *International Journal of Greenhouse Gas Control*, *93*(1), 102899–102908. doi: 10.1016/j.ijggc.2019.102899

Li, J., White, P. R., Bull, J. M., & Leighton, T. G. (2019). A noise impact assessment model for passive acoustic measurements of seabed gas fluxes. *Ocean Engineering*, *183*(1), 294–304. doi: 10.1016/j.oceaneng.2019.03.046

Li, J., White, P. R., Bull, J. M., Leighton, T. G., & Roche, B. (2019). A Model for Variations of Sound Speed and Attenuation from Seabed Gas Emissions. In *MTS/IEEE OCEANS 2019-Seattle, U.S.* (pp. 1–9). doi: 10.23919/OCEANS40490.2019.8962861

Li, J., White, P. R., Roche, B., Bull, J. M., Davis, J. W., Leighton, T. G., ... Cotterle, D. (2019). Natural seabed gas leakage – variability imposed by tidal cycles. In *MTS/IEEE OCEANS 2019-Seattle* (pp. 1–6). doi: 10.23919/OCEANS40490.2019.8962746

Ligtenberg, H., & Connolly, D. (2003). Chimney detection and interpretation, revealing sealing qualityof faults, geohazards, charge of and leakage from reservoirs. *Journal of geochemical exploration*, *78*, 385–387. doi: 10.1016/S0375-6742(03)00095-5

Love, R. H. (1978). Resonant acoustic scattering by swimbladder-bearing fish[a]. *The Journal of the Acoustical Society of America*, *64*(2), 571–580. doi: 10.1121/1.382009

McGinnis, D. F., Greinert, J., Artemov, Y., Beaubien, S., & Wüest, A. (2006). Fate of rising methane bubbles in stratified waters: How much methane reaches the atmosphere? *Journal of Geophysical Research: Oceans*, *111*(C9). doi: 10.1029/2005JC003183

Muyakshin, S., & Sauter, E. (2010). The hydroacoustic method for the quantification of the gas flux from a submersed bubble plume. *Oceanology*, *50*(6), 995–1001. doi: 10.1134/S0001437010060202

Nikolovska, A., Sahling, H., & Bohrmann, G. (2008). Hydroacoustic methodology for detection, localization, and quantification of gas bubbles rising from the seafloor at gas seeps from the eastern Black Sea. *Geochemistry, Geophysics, Geosystems*, *9*(10). doi: 10.1029/2008GC002118

Nikolovska, A., & Schanze, J. (2007). Acoustic methane seepage quantification model design, experiments and deep-sea application. In *IEEE OCEANS 2007-Europe* (pp. 1–6). doi: 10.1109/OCEANSE.2007.4302285

Ochi, H., Watanabe, Y., & Shimura, T. (2008). Measurement of absorption loss at 80 kHz band for wideband underwater acoustic communication. *Japanese Journal of Applied Physics*, *47*(5S), 4366. doi: 10.1143/JJAP.47.4366

Ostrovsky, I. (2003). Methane bubbles in Lake Kinneret: Quantification and temporal and spatial heterogeneity. *Limnology and oceanography*, *48*(3), 1030–1036. doi: 10.4319/lo.2003.48.3.1030

Ostrovsky, I., McGinnis, D. F., Lapidus, L., & Eckert, W. (2008). Quantifying gas ebullition with echosounder: the role of methane transport by bubbles in a medium-sized lake. *Limnology and Oceanography: Methods*, *6*(2), 105–118. doi: 10.4319/lom.2008.6.105

Park, S. H., Park, C., Lee, J., & Lee, B. (2017). A simple parameterization for the rising velocity of bubbles in a liquid pool. *Nuclear Engineering and Technology*, *49*(4), 692–699. doi: 10.1016/j.net.2016.12.006

Riedel, M., Scherwath, M., Römer, M., Veloso, M., Heesemann, M., & Spence, G. (2018). Distributed natural gas venting offshore along the Cascadia margin. *Nature Communications*, *9*(1), 3264. doi: 10.1038/s41467-018-05736-x

Römer, M., Sahling, H., Pape, T., dos Santos Ferreira, C., Wenzhöfer, F., Boetius, A., & Bohrmann, G. (2014). Methane fluxes and carbonate deposits at a cold seep area of the Central Nile Deep Sea Fan, Eastern Mediterranean Sea. *Marine Geology*, *347*, 27–42. doi: 10.1016/j.margeo.2013.10.011

Römer, M., Sahling, H., Spieß, V., & Bohrmann, G. (2011). The role of gas bubble emissions at deep-water cold seep systems: an example from the Makran continental margin, offshore Pakistan. In *Proceedings of the 7th International Conference on Gas Hydrates (ICGH 2011), Edinburgh, Scotland, United Kingdom.*

Rona, P., & Light, R. (2011). Sonar images hydrothermal vents in seafloor observatory. *Eos, Transactions American Geophysical Union*, *92*(20), 169–170. doi: 10.1029/2011EO200002

Ruppel, C. D. (2011). Methane hydrates and contemporary climate change. *Nature Eduction Knowledge*, *2*(12), 12.

Sahling, H., Bohrmann, G., Artemov, Y. G., Bahr, A., Brüning, M., Klapp, S. A., … others (2009). Vodyanitskii mud volcano, Sorokin trough, Black Sea: Geological characterization and quantification of gas bubble streams. *Marine and Petroleum Geology*, *26*(9), 1799–1811. doi: 10.1016/j.marpetgeo.2009.01.010

Salomatin, A., & Yusupov, V. (2005). Quantitative estimation of gas plume parameters by echo-sounder. *Proc. of the XVI Session of the Russian Acoustical Society, Moscow*, 455–458.

Sebastian, T. B., Klein, P. N., & Kimia, B. B. (2003). On aligning curves. *IEEE Transactions on Pattern Analysis and Machine Intelligence*, *25*(1), 116–125. doi: 10.1109/TPAMI.2003.1159951

Shakhova, N., Semiletov, I., Leifer, I., Sergienko, V., Salyuk, A., Kosmach, D., … others (2014). Ebullition and storm-induced methane release from the East Siberian Arctic Shelf. *Nature Geoscience*, *7*(1), 64. doi: 10.1038/ngeo2007

Shakhova, N., Semiletov, I., Salyuk, A., Yusupov, V., Kosmach, D., & Gustafsson, Ö. (2010). Extensive methane venting to the atmosphere from sediments of the East Siberian Arctic Shelf. *Science*, *327*(5970), 1246–1250. doi: 10.1126/science.1182221

Shakhova, N., Semiletov, I., Sergienko, V., Lobkovsky, L., Yusupov, V., Salyuk, A., … others (2015). The East Siberian Arctic Shelf: towards further assessment of permafrost-related methane fluxes and role of sea ice. *Philosophical Transactions of the Royal Society A: Mathematical, Physical and Engineering Sciences*, *373*(2052), 20140451. doi: 10.1098/rsta.2014.0451

Smailes, I. (1976). Observations of volume scattering strength in the northeast atlantic. *The Journal of the Acoustical Society of America*, *60*(5), 1056–1060. doi: 10.1121/1.381196

Sommer, S., Schmidt, M., & Linke, P. (2015). Continuous inline mapping of a dissolved methane plume at a blowout site in the Central North Sea UK using a membrane inlet mass spectrometer–Water column stratification impedes immediate methane release into the atmosphere. *Marine and Petroleum Geology*, *68*, 766–775. doi: 10.1016/j.marpetgeo.2015.08.020

Sündermann, J., & Pohlmann, T. (2011). A brief analysis of North Sea physics. *Oceanologia*, *53*(3), 663–689. doi: 10.5697/oc.53-3.663

Thuraisingham, R. (1997). New expressions of acoustic cross-sections of a single bubble in the monopole bubble theory. *Ultrasonics*, *35*(5), 407–409. doi: 10.1016/S0041-624X(97)00021-8

Toramaru, A. (1989). Vesiculation process and bubble size distributions in ascending magmas with constant velocities. *Journal of Geophysical Research: Solid Earth*, *94*(B12), 17523–17542. doi: 10.1029/JB094iB12p17523

Urban, P., Köser, K., & Greinert, J. (2017). Processing of multibeam water column image data for automated bubble/seep detection and repeated mapping. *Limnology and Oceanography: Methods*, *15*(1), 1–21. doi: 10.1002/lom3.10138

Veloso, M., Greinert, J., Mienert, J., & De Batist, M. (2015). A new methodology for quantifying bubble flow rates in deep water using splitbeam echosounders: Examples from the Arctic offshore NW-Svalbard. *Limnology and Oceanography: methods*, *13*(6), 267–287. doi: 10.1002/lom3.10024

von Deimling, J. S., Greinert, J., Chapman, N., Rabbel, W., & Linke, P. (2010). Acoustic imaging of natural gas seepage in the North Sea: Sensing bubbles controlled by variable currents. *Limnology and Oceanography: Methods*, *8*(5), 155–171. doi: 10.4319/lom.2010.8.155

von Deimling, J. S., Linke, P., Schmidt, M., & Rehder, G. (2015). Ongoing methane discharge at well site 22/4b (North Sea) and discovery of a spiral vortex bubble plume motion. *Marine and Petroleum Geology*, *68*, 718–730. doi: 10.1016/j.marpetgeo.2015.07.026

von Deimling, J. S., Rehder, G., Greinert, J., McGinnnis, D., Boetius, A., & Linke, P. (2011). Quantification of seep-related methane gas emissions at Tommeliten, North Sea. *Continental Shelf Research*, *31*(7-8), 867–878. doi: 10.1016/j.csr.2011.02.012

Westbrook, G. K., Thatcher, K. E., Rohling, E. J., Piotrowski, A. M., Pälike, H., Osborne, A. H., . . . others (2009). Escape of methane gas from the seabed along the West Spitsbergen continental margin. *Geophysical Research Letters*, *36*(15). doi: 10.1029/2009GL039191

Xia, M., & Liu, B. (2004). Image registration by "Super-curves". *IEEE Transactions on Image Processing*, *13*(5), 720–732. doi: 10.1109/TIP.2003.822611

Xu, C., Wu, M., Zhou, T., Li, J., Du, W., Zhang, W., & White, P. R. (2020). Optical Flow-Based Detection of Gas Leaks from Pipelines Using Multibeam Water Column Images. *Remote Sensing*, *12*(1), 119–139. doi: 10.3390/rs12010119

Xu, G., Jackson, D. R., Bemis, K. G., & Rona, P. A. (2014). Time-series measurement of hydrothermal heat flux at the Grotto mound, Endeavour Segment, Juan de Fuca Ridge. *Earth and Planetary Science Letters*, *404*, 220–231. doi: 10.1016/j.epsl.2014.07.040

Figure1.

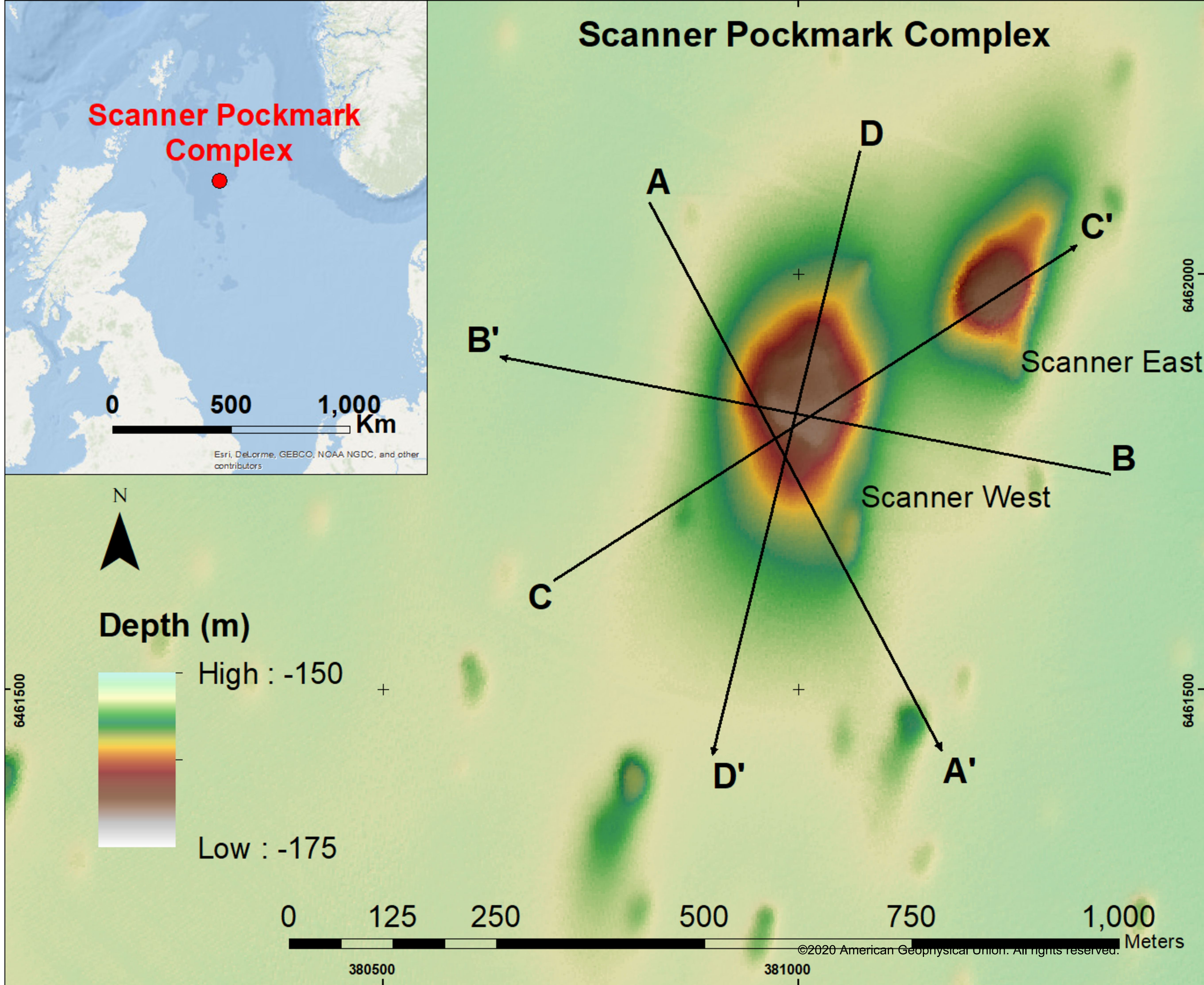

Scanner Pockmark Complex
Scanner Pockmark
Complex
0
500
1,000
Km
Esri, DeLorme, GEBCO, NOAA NGDC, and other contributors
N
Depth (m)
High : -150
Low : -175
A
A'
B
B'
C
C'
D
D'
Scanner East
Scanner West
6462000
6461500
6461500
0
125
250
500
750
1,000
Meters
380500
381000

Figure2.

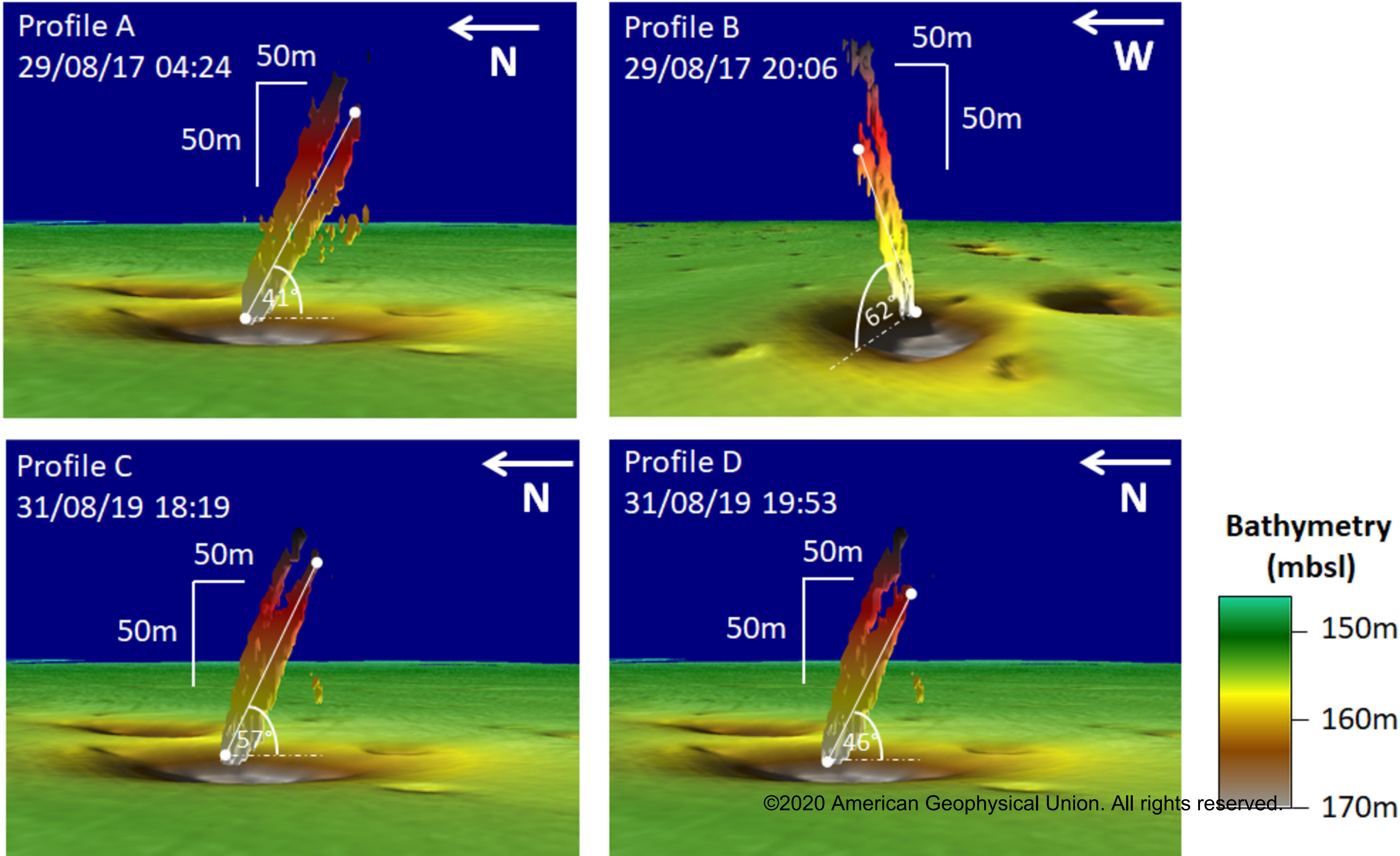
Profile A
29/08/17 04:24
N
50m
50m
41°
Profile B
29/08/17 20:06
W
50m
50m
62°
Profile C
31/08/19 18:19
N
50m
50m
57°
Profile D
31/08/19 19:53
N
50m
50m
46°
Bathymetry (mbsl)
150m
160m
170m

Figure3.

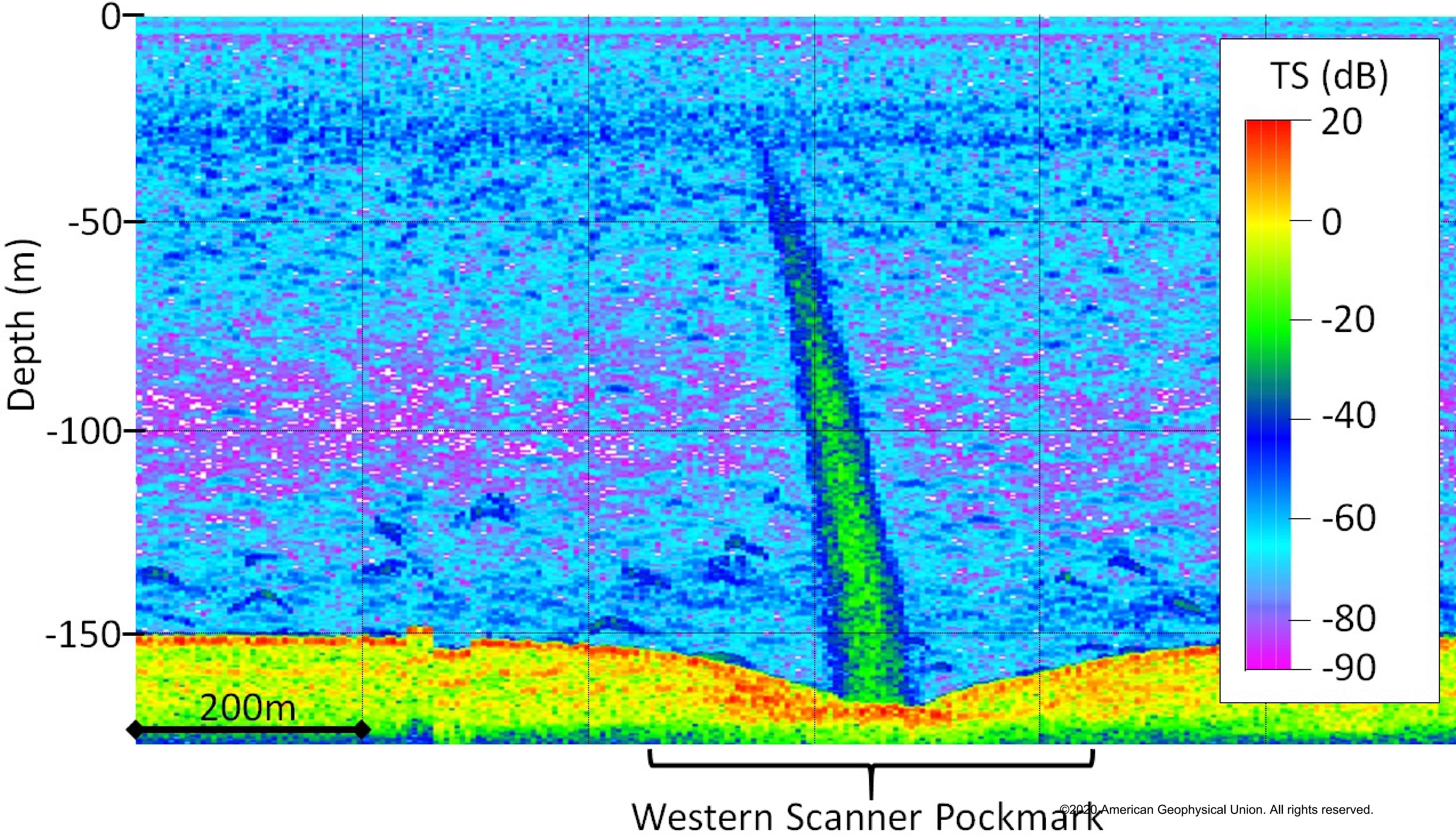
0
-50
-100
-150
Depth (m)
200m
TS (dB)
20
0
-20
-40
-60
-80
-90
Western Scanner Pockmark

Figure4.

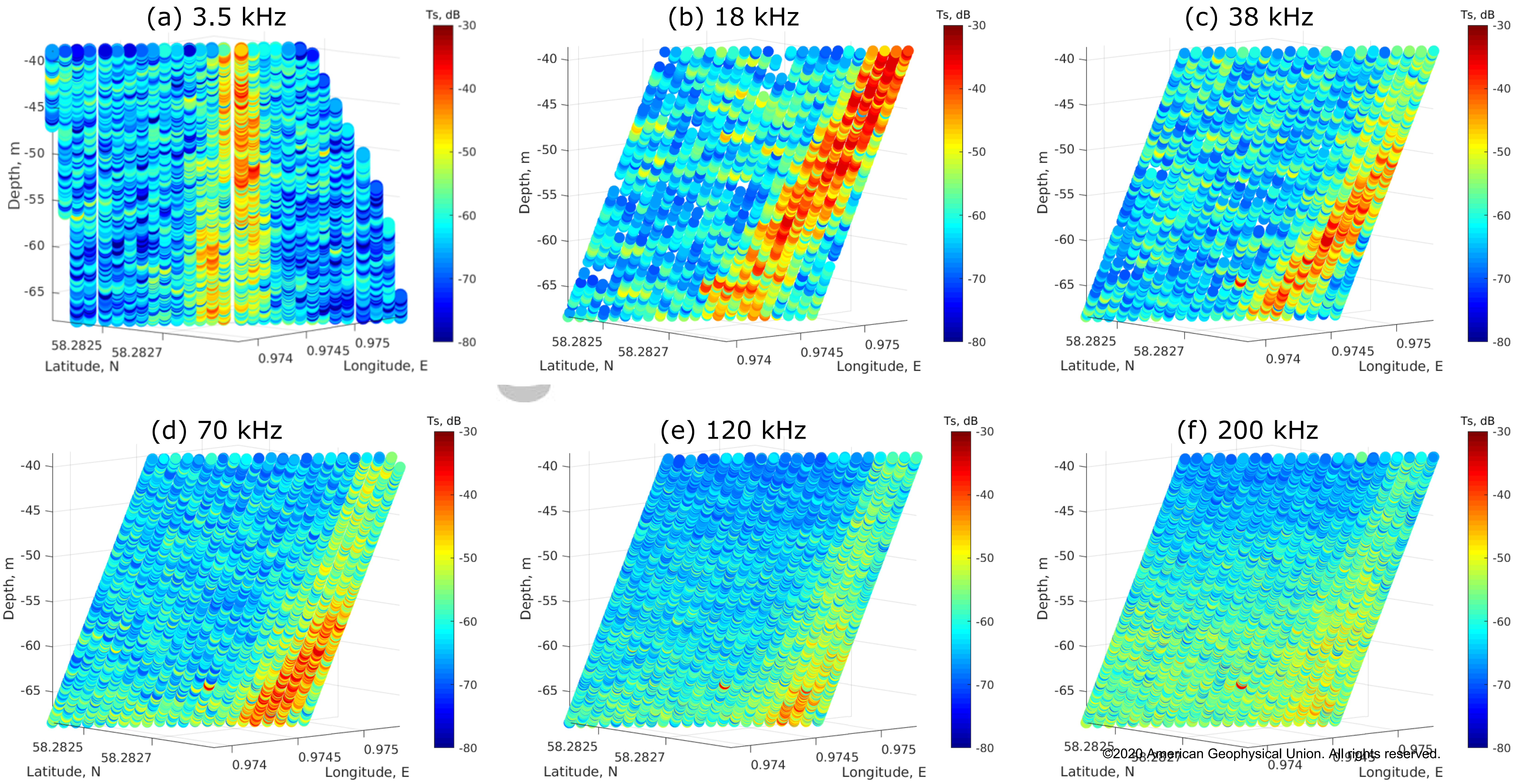
(a) 3.5 kHz
(b) 18 kHz
(c) 38 kHz
(d) 70 kHz
(e) 120 kHz
(f) 200 kHz
Ts, dB
-30
-40
-50
-60
-70
-80
Depth, m
-40
-45
-50
-55
-60
-65
58.2825
58.2827
Latitude, N
0.974
0.9745
0.975
Longitude, E

Figure5.

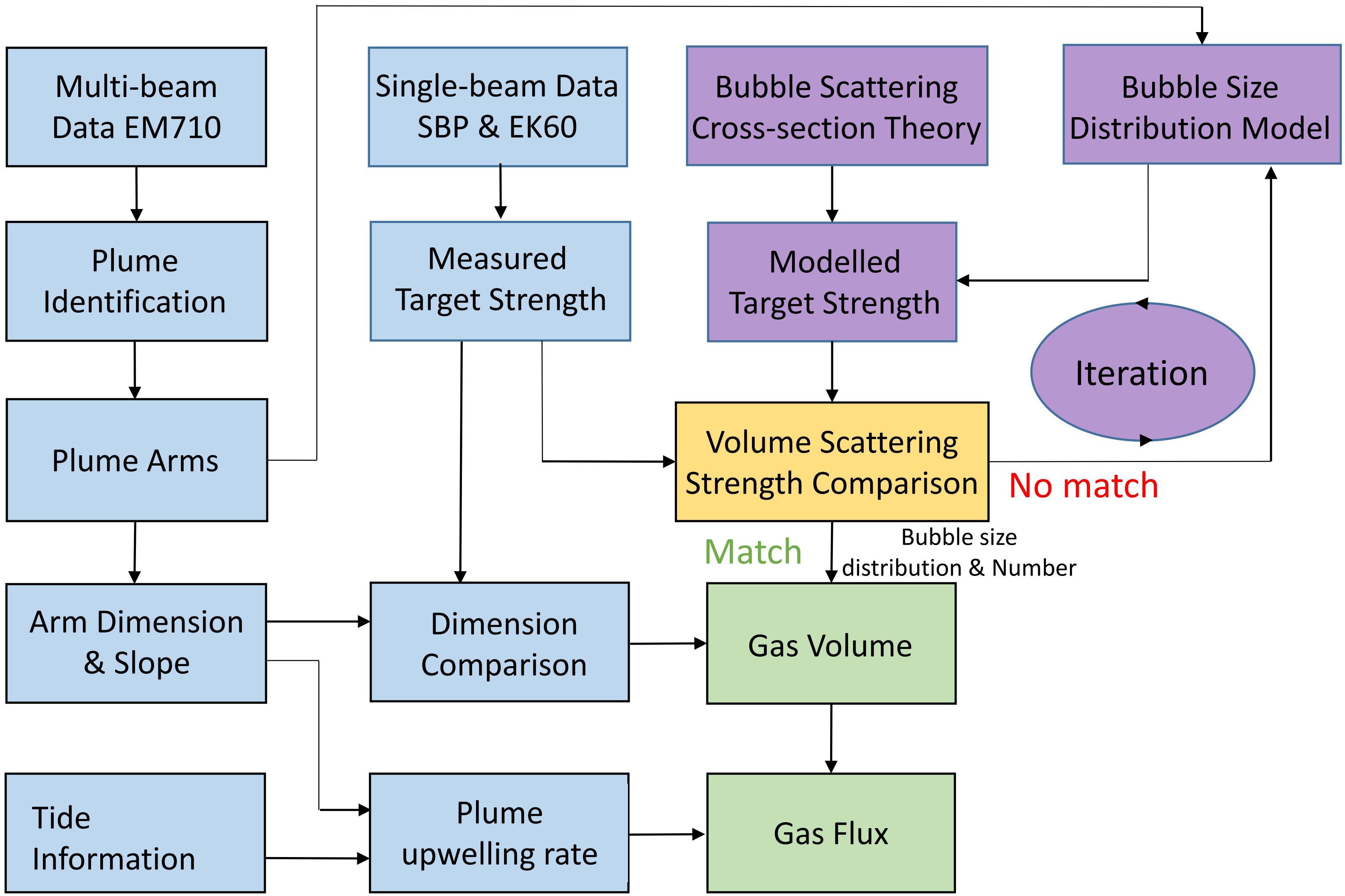

Multi-beam Data EM710
Single-beam Data SBP & EK60
Bubble Scattering Cross-section Theory
Bubble Size Distribution Model
Plume Identification
Measured Target Strength
Modelled Target Strength
Iteration
Plume Arms
Volume Scattering Strength Comparison
No match
Match
Bubble size distribution & Number
Arm Dimension & Slope
Dimension Comparison
Gas Volume
Tide Information
Plume upwelling rate
Gas Flux

Figure6.

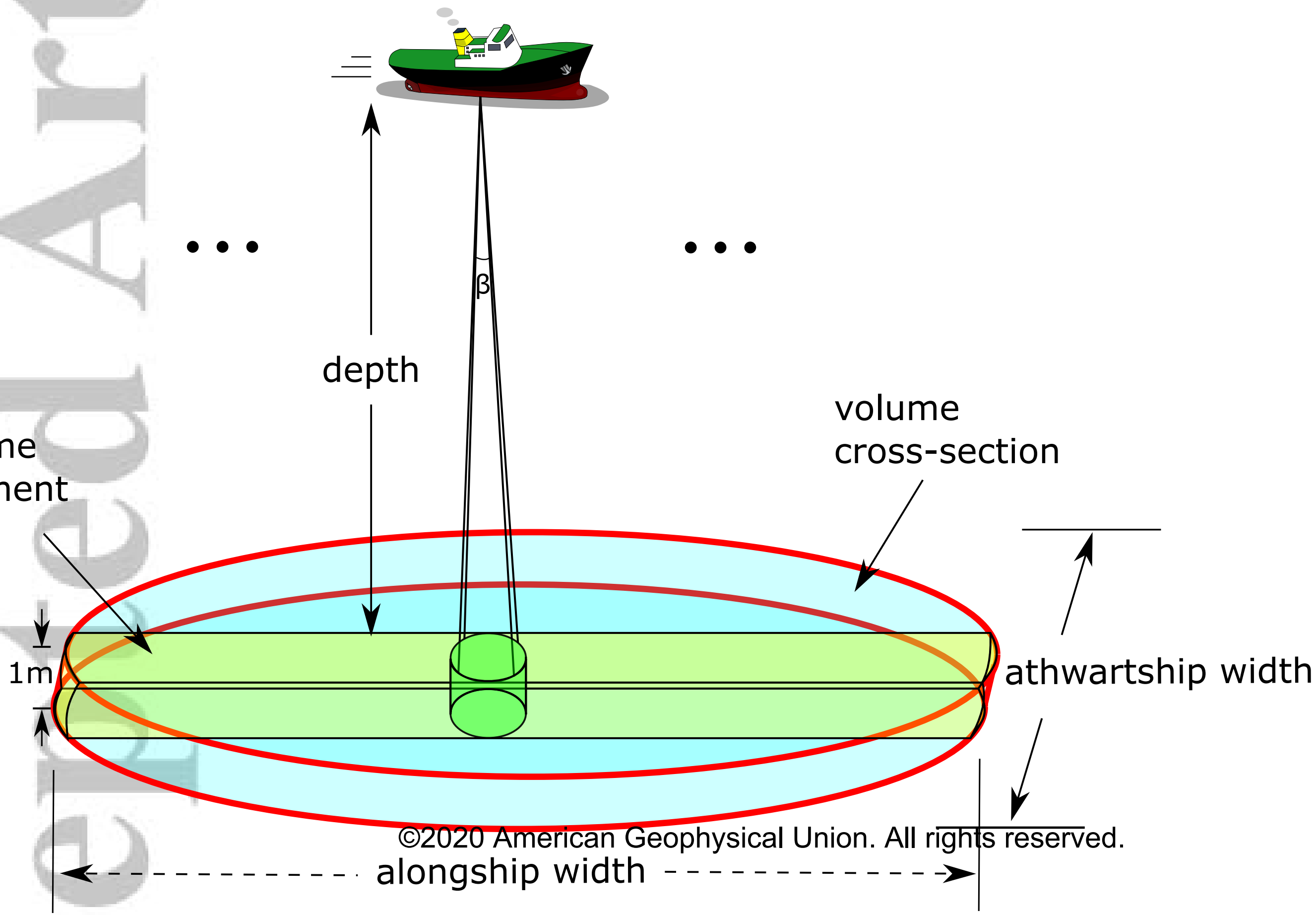
depth
β
volume
cross-section
volume
fragment
1m
athwartship width
alongship width

Figure7.

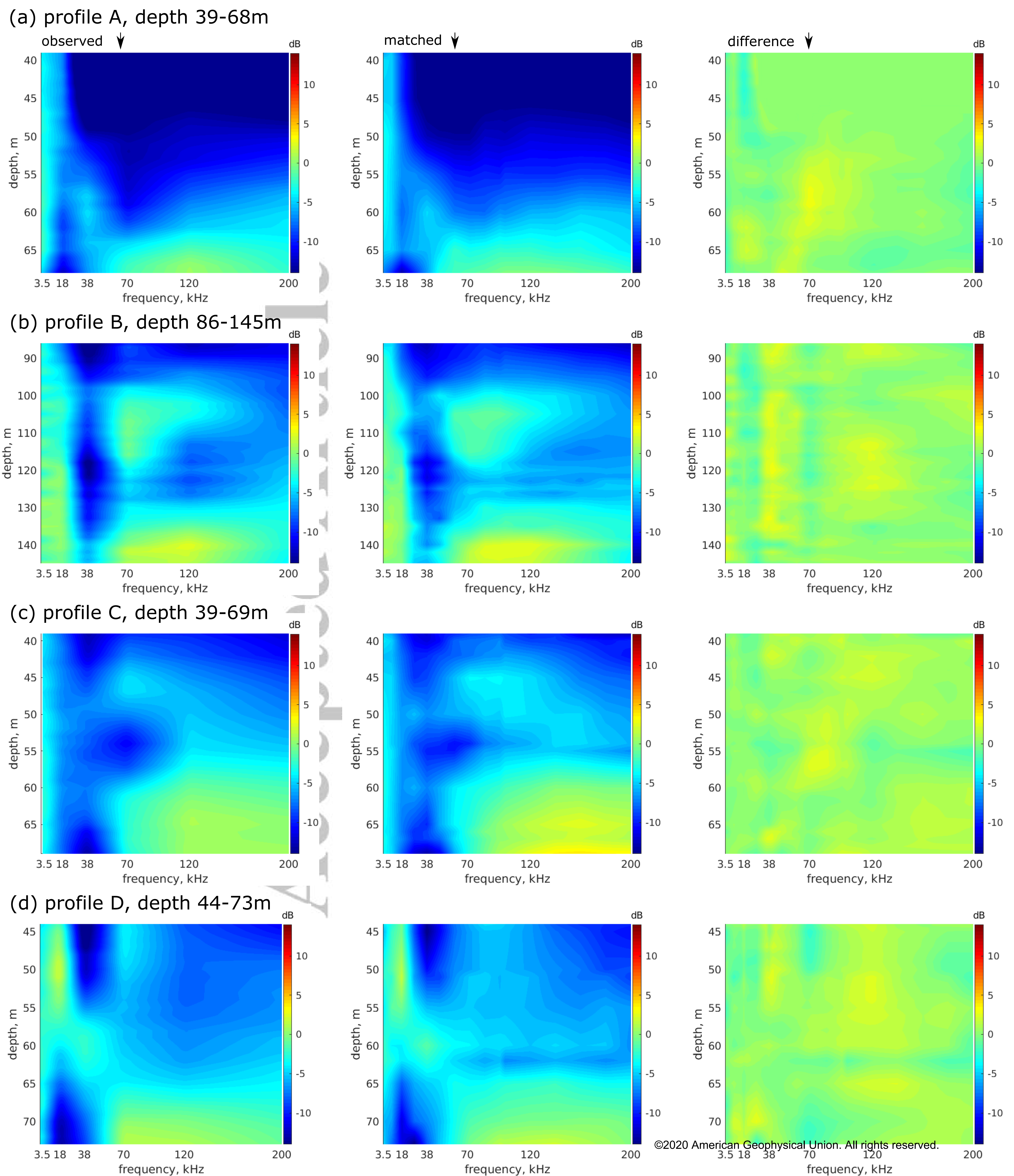
(a) profile A, depth 39-68m
observed
matched
difference
(b) profile B, depth 86-145m
(c) profile C, depth 39-69m
(d) profile D, depth 44-73m
depth, m
frequency, kHz
dB
3.5 18 38 70 120 200

Figure8.

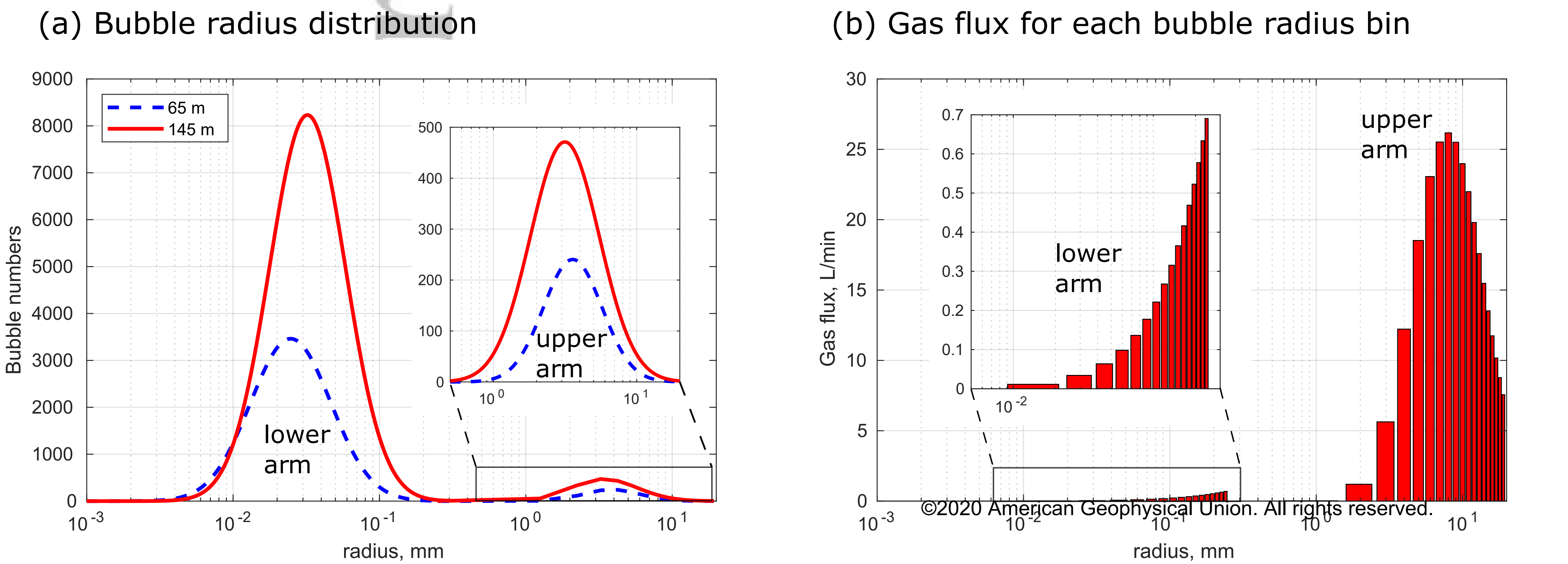

(a) Bubble radius distribution
Bubble numbers
radius, mm
65 m
145 m
lower arm
upper arm
(b) Gas flux for each bubble radius bin
Gas flux, L/min
radius, mm
lower arm
upper arm

Figure9.

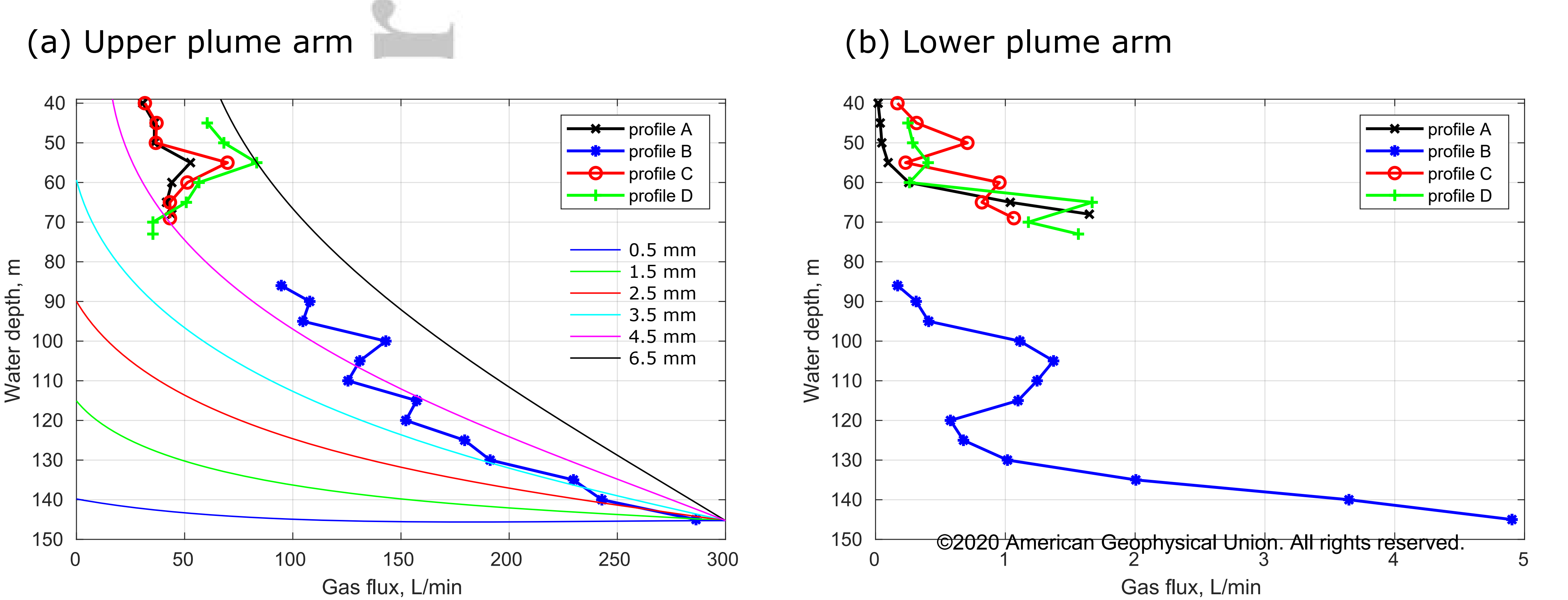
(a) Upper plume arm
(b) Lower plume arm
profile A
profile B
profile C
profile D
0.5 mm
1.5 mm
2.5 mm
3.5 mm
4.5 mm
6.5 mm
Water depth, m
Gas flux, L/min
40
50
60
70
80
90
100
110
120
130
140
150
0
50
100
150
200
250
300
1
2
3
4
5